UC Irvine

Title

A Study of the 20 day Superorbital Modulation in the High-mass X-Ray Binary IGR J16493-4348

Permalink

https://escholarship.org/uc/item/2jw089fn

Journal

The Astrophysical Journal, 879(1)

ISSN

0004-637X

Authors

Coley, Joel B
Corbet, Robin HD
Fürst, Felix
et al.

Publication Date

2019-07-01

DOI

10.3847/1538-4357/ab223c
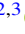
Copyright Information

Peer reviewed

A Study of the 20 day Superorbital Modulation in the High-mass X-Ray Binary IGR J16493-4348

Joel B. Coley[1,2] , Robin H. D. Corbet[3,4] , Felix Fürst[5] , Gregory Huxtable[3,4], Hans A. Krimm[6,7] ,
Aaron B. Pearlman[8,9,10] , and Katja Pottschmidt[2,3]

[1] Department of Physics and Astronomy, Howard University, Washington, DC 20059, USA; joel.coley@howard.edu
[2] CRESST/Mail Code 661, Astroparticle Physics Laboratory, NASA Goddard Space Flight Center, Greenbelt, MD 20771, USA
[3] University of Maryland, Baltimore County, MD, USA
[4] CRESST/Mail Code 662, X-ray Astrophysics Laboratory, NASA Goddard Space Flight Center, Greenbelt, MD 20771, USA
[5] European Space Astronomy Center (ESA/ESAC), Operations Department, Vilanueva de la Cañada (Madrid), Spain
[6] Universities Space Research Association, Columbia, MD 21046, USA
[7] National Science Foundation, Alexandria, VA 22314, USA
[8] Division of Physics, Mathematics, and Astronomy, California Institute of Technology, Pasadena, CA 91125, USA

Abstract

We report on *Nuclear Spectroscopic Telescope Array (NuSTAR)*, *Neil Gehrels Swift Observatory* (*Swift*) X-ray Telescope (XRT), and *Swift* Burst Alert Telescope (BAT) observations of IGR J16493-4348, a wind-fed supergiant X-ray binary showing significant superorbital variability. From a discrete Fourier transform of the BAT light curve, we refine its superorbital period to be 20.058 ± 0.007 days. The BAT dynamic power spectrum and a fractional root mean square analysis both show strong variations in the amplitude of the superorbital modulation, but no observed changes in the period are found. The superorbital modulation is significantly weaker between MJD 55,700 and MJD 56,300. The joint *NuSTAR* and XRT observations, which were performed near the minimum and maximum of one cycle of the 20 day superorbital modulation, show that the flux increases by more than a factor of two between superorbital minimum and maximum. We find no significant changes in the 3–50 keV pulse profiles between superorbital minimum and maximum, which suggests a similar accretion regime. Modeling the pulse-phase-averaged spectra we find a possible Fe Kα emission line at 6.4 keV at superorbital maximum. This feature is not significant at superorbital minimum. While we do not observe any significant differences between the pulse-phase-averaged spectral continua apart from the overall flux change, we find that the hardness ratio near the broad main peak of the pulse profile increases from superorbital minimum to maximum. This suggests the spectral shape hardens with increasing luminosity. We discuss different mechanisms that might drive the observed superorbital modulation.

Key words: accretion, accretion disks – stars: individual (IGR J16493-4348) – stars: neutron – X-rays: binaries

1. Introduction

IGR J16493-4348 is a high-mass X-ray binary first discovered during a survey of the Galactic plane using the *INTErnational Gamma-Ray Astrophysics Laboratory* (*INTEGRAL*; Winkler et al. 2003) satellite (Bird et al. 2004). During a deep scan of the Norma Arm region using *INTEGRAL*, it was later identified by Grebenev et al. (2005) to be a variable source with a mean photon flux of 5.6 ± 0.6 mCrab in the 18–45 keV energy band. Two pointed observations using the *Rossi X-ray Timing Explorer (RXTE)* Proportional Counter Array (PCA) revealed the mean X-ray spectrum to be consistent with a highly absorbed power law. Its photon index and neutral hydrogen absorbing column were found to be 1.4 and $\sim 10^{23}$ cm^{-2}, respectively (Markwardt et al. 2005).

A spectral analysis using the *Neil Gehrels Swift Observatory* (*Swift*) Burst Alert Telescope (BAT) and the *INTEGRAL* Soft Gamma-ray Imager (ISGRI), together with pointed *Swift* X-ray Telescope (XRT) and *Suzaku* observations, revealed a hint of an absorption feature at 33 ± 4 keV thought to be a cyclotron resonant scattering feature (CRSF), implying a magnetic field of $(3.7 \pm 0.4) \times 10^{12}$ G (D'Aì et al. 2011). The width of the absorption feature was found to be 10 keV.

A single source in the Two Micron All-Sky Survey (2MASS) catalog, 2MASS J16492695-4349090, was identified as the infrared counterpart (Kuiper et al. 2005). Using the European Southern Observatory Infrared Spectrometer and Array Camera spectrograph on UT1 at Paranal observatory, Nespoli et al. (2010) proposed the spectral type of the donor star to be B0.5–1 Ia–Ib. The distance to the source was estimated to be between 6 and 26 kpc by Nespoli et al., but could not be tightly constrained due to the uncertainty of the intrinsic colors.

A ∼6.78 day orbital period was independently found by Corbet et al. (2010a) and Cusumano et al. (2010). It was later refined by Corbet & Krimm (2013) to be 6.782 ± 0.001 days using the BAT Transient Monitor. The neutron star is regularly eclipsed by the donor star for about 0.8 days of every orbit, which indicates the orbital inclination is close to edge-on (Pearlman et al. 2019). From an eclipse timing analysis using the *Swift* BAT and *RXTE* PCA, Pearlman et al. (2019) further refined the orbital period to be 6.7828 ± 0.0004 days.

Recently, Pearlman et al. (2019) placed constraints on the nature of the donor star using their eclipse timing results. They proposed the spectral type of the donor star and the distance to the source to be B0.5 Ia and 16.1 ± 1.5 kpc, respectively. We adopt these measurements in this work.

Corbet et al. (2010b) found evidence of a ∼1069 s signal using the *RXTE* PCA, which they interpreted as the neutron star

rotation period. From a pulsar timing analysis using an extended PCA data set, this was later refined to 1093.1036 ± 0.0004 s (Pearlman et al. 2019). The epoch of maximum delay time, $T_{\pi/2}$, and pulse period derivative were found to be MJD $55{,}850.91 \pm 0.05$ and $5.4^{+7.9}_{-9.7} \times 10^{-8}$ s s^{-1}, respectively (Pearlman et al. 2019).

In addition to the neutron star rotation and orbital periods, a longer superorbital period was observed from IGR J16493-4348. Using data from the *Swift* BAT 58 month survey and the *RXTE* Galactic plane scans, a $\sim$20 day modulation was found (Corbet et al. 2010a). The superorbital period was later refined to be 20.07 ± 0.01 days using the BAT Transient Monitor (Corbet & Krimm 2013). More recently, Pearlman et al. (2019) refined the superorbital period to be 20.067 ± 0.009 days also using the BAT.

Superorbital modulation was additionally seen in the wind-fed supergiant X-ray binaries (SGXBs) 2S 0114+650 (Farrell et al. 2008), IGR J16418-4532, IGR J16479-4514, and 4U 1909+07 (Corbet & Krimm 2013). More recently, Corbet et al. (2018) reported evidence of superorbital modulation in 4U 1538-522. In their review of wind-fed SGXBs showing strong superorbital modulation, Corbet & Krimm (2013) found a possible correlation between the orbital and superorbital periods of these binaries, but the mechanism to account for this correlation remains unclear. Superorbital variability in wind-fed SGXBs is not a ubiquitous feature since many wind-fed SGXBs show strong orbital modulation but no signs of superorbital modulation (Corbet & Krimm 2013).

In Roche-lobe overflow systems, superorbital variations can typically be explained by X-ray irradiation from a central source illuminating a tilted and/or warped accretion disk, causing it to precess and periodically obscure the compact object from the line of sight (Pringle 1996; Ogilvie & Dubus 2001). Similar variability has also recently been found in ultraluminous X-ray (ULX) pulsars (e.g., NGC 5907 ULX1; NGC 7793 P13; M82 X-2, Walton et al. 2016; Fürst et al. 2018; Brightman et al. 2019). However, the mechanism responsible for the long-timescale modulation in wind-fed SGXBs remains poorly understood. Depending on the angular momentum transferred to the compact object by the stellar wind, accretion in wind-fed SGXBs may be mediated by a quasi-spherical outflow (Bondi & Hoyle 1944) or by an accretion disk-like structure albeit of a transient nature (El Mellah et al. 2019; Taani et al. 2018, 2019). Indeed, transient accretion disks have been observed in some wind-fed SGXBs (e.g., OAO 1657-415, 2S 0114+650; Jenke et al. 2012; Hu et al. 2017). While it is unlikely that a precessing warped and/or tilted accretion disk is the primary mechanism that drives superorbital modulation in wind-fed SGXBs, it is possible that the superorbital variations are caused by a variable mass accretion rate. Possible mechanisms that could drive superorbital variations in wind-fed SGXBs include neutron star precession (Postnov et al. 2013), donor star variability (Koenigsberger et al. 2006), or the presence of a third star in a hierarchical system (Chou & Grindlay 2001). Recently, Bozzo et al. (2017) proposed that a corotation interaction region with a period of $\sim$10.3 days could explain the $\sim$20.07 day superorbital period and amplitude in IGR J16493-4348.

In this paper, we analyze two *Nuclear Spectroscopic Telescope Array* (*NuSTAR*) and *Swift* XRT observations of IGR J16493-4348 near the maximum and the minimum of one cycle of the $\sim$20 day superorbital modulation, together with *Swift* BAT Transient Monitor observations, which track the evolution of the superorbital modulation on long timescales. The remainder of the paper is organized as follows. *NuSTAR* and *Swift* observations are presented in Section 2. Section 3.1 focuses on long-term monitoring of the $\sim$20 day superorbital modulation with the *Swift* BAT. In Section 3.2, we measure the neutron star rotation period using the *NuSTAR* X-ray telescope and show pulse profiles and their energy dependence at superorbital minimum and superorbital maximum. Pulse-phase-averaged and phase-resolved spectral results are given in Sections 3.3 and 3.4, respectively. Section 3.5 focuses on the spectroscopy at the peak of the pulse profile. We provide a discussion of the results in Section 4 and the conclusions are given in Section 5. Unless stated otherwise, the uncertainties and limits presented in the paper are at the 90% confidence level.

2. Data and Analysis

The observations outlined below consist of nearly simultaneous *NuSTAR* and *Swift* XRT observations during superorbital minimum (2015 August 31–September 1) and superorbital maximum (2015 September 12), as well as long-term observations of the system with the *Swift* BAT. An observation log is given in Table 1.

2.1. NuSTAR *Observations*

NuSTAR (Harrison et al. 2013) carries two co-aligned grazing incidence Wolter I imaging telescopes that focus X-rays between 3 and 79 keV onto two independent solid state Focal Plane Modules (hereafter FPMA and FPMB). We reduced and screened the data using the *NuSTAR* Data Analysis Software (NuSTARDAS) v.1.7.0 package provided under HEAsoft v.6.20 and calibration files dated 2016 December 7. The data were reprocessed with the NuSTARDAS data pipeline package `nupipeline` using the standard filtering procedure to apply the newest calibration and default screening criteria.

The source spectra were extracted in mode 01 (`SCIENCE`) from a circular region of radius $60\rlap{.}''0$ centered on the source. Since the Norma Arm is a crowded region, we checked for stray light contamination produced by sources outside the field of view using the scripts made available on the *NuSTAR* GitHub webpage.[11] We found that FPMA is affected by stray light from multiple sources. To investigate variations in the background due to stray light, we tested different background regions on the same detector as the source while avoiding visible stray light. We found the spectral parameters do not significantly depend on the choice of background (see Sections 3.3–3.5). This is not surprising since IGR J16493-4348 was found to be a factor of 10 times brighter than the background at energies below 30 keV and a factor of two at energies above 30 keV. We therefore chose to extract a background from a circular region of radius $60\rlap{.}''0$ offset from the source. Event times were corrected to the solar system barycenter using `nuproducts` and the FTOOL `barycorr` with the DE-200 solar system ephemeris. For the timing analysis and pulse-phase-resolved spectra, we further corrected the event times for the orbital motion of the neutron star using the ephemeris defined in Pearlman et al. (2019), which

---

[11] https://github.com/NuSTAR

Table 1
Summary of X-Ray Observations of IGR J16493-4348

Obs.	Telescope	ObsID	Start Time (UT)	End Time (UT)	Orbital Phase[a]	Superorbital Phase[b]	Exposure (ks)
Min	*NuSTAR*	30102054004	2015 Aug 31 07:23:41	2015 Sep 01 00:26:38	0.527–0.632	0.520–0.555	31.2
Max	*NuSTAR*	30102054006	2015 Sep 12 04:40:20	2015 Sep 12 15:17:55	0.280–0.344	1.113–1.135	21.6
Min	*Swift*	00081665002	2015 Aug 31 10:25:51	2015 Aug 31 10:34:38	0.545–0.546	0.526–0.527	0.5[c]
Max	*Swift*	00081665003	2015 Sep 12 13:00:01	2015 Sep 12 14:56:54	0.331–0.343	1.130–1.134	1.9[c]

Notes.
[a] Orbital phase zero is defined at MJD 55,851.2, corresponding to the epoch of maximum delay time, $T_{\pi/2}$ (Pearlman et al. 2019).
[b] Superorbital phase zero is defined as the epoch of maximum flux (MJD 57,254.9 ± 0.3).
[c] Net exposure time is spread over several snapshots.

assumed a circular orbital solution and no change in the neutron star rotation period (see Section 1). For phase-resolved spectra, good time intervals were generated using the `nuproducts` tool and the "usrgtifile" keyword. Response matrices were generated using the packages `numkarf` and `numkrmf`.

The net count rates from the source over the full energy range were found to be 0.595 ± 0.004 counts s^{-1} (FPMA) and 0.571 ± 0.004 counts s^{-1} (FPMB) at superorbital minimum and 1.679 ± 0.009 counts s^{-1} (FPMA) and 1.651 ± 0.009 counts s^{-1} (FPMB) at superorbital maximum. The background was found to dominate at energies exceeding ∼40 keV at superorbital minimum and ∼50 keV at superorbital maximum. As a result, we chose to analyze the spectra between 3–40 keV. We rebinned the spectral file produced by `nuproducts` to have a minimum of 50 counts per bin using `grppha`.

2.2. Swift

2.2.1. XRT Observations

The *Swift* XRT (Burrows et al. 2005) is a Wolter I imaging telescope sensitive to X-rays ranging from 0.3 to 10 keV. We reduced and screened the data using the HEAsoft v.6.20 package and calibration files dated 2017 May 1, following the procedures defined in the XRT Data Reduction Guide (Capalbi et al. 2005). The data were reprocessed with the XRTDAS standard data pipeline package `xrtpipeline` using the standard filtering procedure to apply the newest calibration and default screening criteria. All data were taken in photon counting (PC; Hill et al. 2004) mode with a data readout time of 2.5 s, adopting the standard grade filtering (0–12 for PC).

We found the non-background-subtracted count rates at superorbital minimum and superorbital maximum to be 0.15 ± 0.01 counts s^{-1} and 0.25 ± 0.01 counts s^{-1}, respectively. Since our observations of IGR J16493-4348 were not affected by pile-up, we extracted the source spectra from circular regions of radius 30″ centered on the source. The backgrounds were extracted from an annular region of internal radius 60″ and external radius 120″ centered on the source. The ancillary response files, accounting for vignetting, point-spread function correction, and different extraction regions, were generated and corrected for exposure using the FTOOL packages `xrtmkarf` and `xrtexpomap`, respectively.

We further processed the spectral data produced by `xselect` using the FTOOL `grppha`, which defined the binning and quality flags of the spectra. We used the quality flag to further eliminate bad data. Bins were grouped to ensure a minimum of 20 counts per bin.

2.2.2. BAT Observations

The BAT, on board the *Swift* spacecraft, is a hard X-ray telescope operating in the 14–195 keV energy band (Barthelmy et al. 2005). It provides an all-sky hard X-ray survey with a sensitivity of ∼1 mCrab (Tueller et al. 2010). We analyzed BAT data obtained during the time period MJD 53,416–57,923 (2005 February 15–2017 June 19). Light curves were retrieved using the extraction of the BAT Transient Monitor data available on the NASA GSFC HEASARC website[12] (Krimm et al. 2013). We used the orbital light curves in the 15–50 keV energy band in our analysis, which have exposures that range from 64 to 2640 s in each time bin (see Section 3.1). The mean exposure in the time bins was 706 s. The short exposures can arise due to the observing plan of *Swift* since the BAT is primarily tasked to observe gamma-ray bursts (Krimm et al. 2013).

The light curves were further screened to exclude bad quality points. We only considered data where the data quality flag ("DATA_FLAG") was set to 0, indicating good quality. Data flagged as "good" are sometimes suspect, where a small number of data points with very low fluxes and implausibly small uncertainties are found (Corbet & Krimm 2013). These points were removed from the light curves. We corrected the photon arrival times to the solar system barycenter using the scripts made available on the Ohio State Astronomy webpage.[13]

3. Results

3.1. Long-term Variability

The *Swift* BAT Transient Monitor light curve of IGR J16493-4348 is shown in Figure 1. We rebinned the light curve to two superorbital cycles and found no major variability over the duration of the light curve.

We derived the superorbital period using a discrete Fourier transform (DFT) of the BAT light curve, after removing points that fell within the eclipse of the neutron star from the start of ingress to the end of egress using the ephemeris defined in Pearlman et al. (2019). The DFT covered a period range between 0.07 days and the length of the light curve—i.e., ∼4507 days. We weighted the contribution of each data point

---

[12] http://heasarc.gsfc.nasa.gov/docs/swift/results/transients/
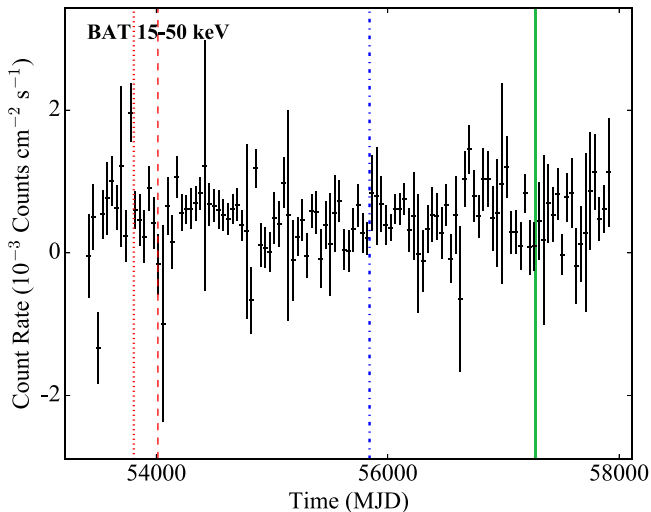[13] http://astroutils.astronomy.ohio-state.edu/time/

Figure 1. Long-term *Swift* BAT light curve of IGR J16493-4348 in the 15–50 keV band (MJD 53,416–57,923). The light curve is binned to a time resolution chosen to be two superorbital cycles (∼40.13 days). The superorbital cycle coinciding with the times of the *NuSTAR* observations is indicated by the green shaded region. The *Swift* XRT, *Suzaku*, and *RXTE* PCA observations reported in Hill et al. ([2008](#)), Morris et al. ([2009](#)), and Pearlman et al. ([2019](#)), respectively, are indicated by the dotted red, dashed red, and dotted–dashed blue lines, respectively.

by its uncertainty when calculating the power spectrum using the "semi-weighting" technique (Corbet et al. [2007](#); Corbet & Krimm [2013](#)), where the error bars on each data point and the excess variability of the light curve are taken into account. The significance of the peak at the superorbital period was estimated using the false-alarm probability (FAP; Scargle [1982](#)), which depends on the number of independent frequencies and therefore the nominal frequency resolution. While this is not precisely defined for unevenly sampled data (Koen [1990](#)), the inverse of the light-curve length provides a reasonable approximation (Corbet et al. [2017](#)). The uncertainty in our period measurements is obtained using the expression given in Horne & Baliunas ([1986](#)).

The ∼20 day superorbital modulation is strongly detected in the DFT of the BAT Transient Monitor light curve. Using an additional 674 days of data compared to Pearlman et al. ([2019](#)), we refine the superorbital period to 20.058 ± 0.007 days (see Figure [2](#)(c)). The FAP is 3×10^{-7}. We note that by excising the eclipses, gaps with a spacing of about 1.7 days are created in the light curve, which could possibly lead to aliasing effects in the power spectrum. To investigate this, we created a light curve using the times of the BAT light and replaced the data values with a sinusoidal modulation at 20.058 days. We found no evidence of aliasing in the power spectrum.

To monitor changes in the ∼20.06 day modulation, we constructed dynamic power spectra using the *Swift* BAT light curve (see Figure [2](#)(a)). To investigate whether changes in the signal were sudden or gradual, overlapping light curve subsets were used (e.g., Clarkson et al. [2003](#)). We divided the light curve into 70 data windows, each with a length of 1000 days, that were successively shifted in time by 50 days relative to each other. We calculated the DFT from each subset of data. In Figure [2](#)(a), we show that the amplitude of the ∼20.06 day modulation changes as a function of time. We find no change in the period of the ∼20.06 day modulation.

In Figure [2](#)(b), we show changes in the strength of the ∼20.06 day modulation relative to the average value for each

of the individual 70 power spectra. We find the peak power to be more than 10 times the mean power up to ∼MJD 54,300 and again at MJD 55,000–55,200 (2009 September 26–2010 January 4). The relative peak height is found to be near constant at five times the mean power level between MJD 54,300–55,000. From MJD 55,500 to MJD 56,100 (2012 June 22), we find that it decreases, reaching a minimum of 1.3 times the mean power level. The power then increases linearly up to MJD 56,400 (2013 April 18) where it is again larger than five times the mean power level.

Quasi-sinusoidal behavior was found in the BAT Transient Monitor light curve folded on the superorbital period (see Figure [3](#)(c)) where we defined phase zero as the epoch of the maximum flux derived from a sine wave fit. Since the *NuSTAR* observation near superorbital minimum began at MJD 57,265.3 (see Table [1](#)), we express the epoch of maximum flux (MJD $57,254.9 \pm 0.3$) at an epoch closest to the *NuSTAR* observation assuming no appreciable change in the superorbital period.

We investigated changes in the amplitude and phase of the superorbital modulation using a dynamic folded light curve (see Figure [3](#)(a)). We divided the light curve into 70 data windows, which each had a length of 1000 days and were shifted in time by 50 days relative to each other. We folded the light curve from each subset of data on the 20.058 ± 0.007 day period. The dynamic folded light curve shows a maximum and minimum near superorbital phases ∼0.9–0.2 and ∼0.4–0.6, respectively.

To further investigate changes in the amplitude of the modulation, we calculated the fractional root mean square (rms) amplitude and its uncertainty for each 1000 day segment using Equations (10) and (B2) in Vaughan et al. ([2003](#)), respectively (see Figure [3](#)(b)). We find the fractional rms amplitude to track the power of the ∼20.06 day modulation as a function of time. The fractional rms analysis shows the amplitude of the superorbital modulation significantly decreased to less than 3% between MJD 55,700 and MJD 56,300, which is consistent with the weakening in the dynamic power spectrum. The weighted Pearson correlation coefficient between the fractional rms and relative height is found to be $r = 0.83$, with a probability of arising by chance of 5×10^{-8}.

3.2. Short-term Temporal Analysis

In Figure [4](#)(a), we show the *Swift* BAT light curve folded on the 20.058 ± 0.007 day superorbital period using the ephemeris defined in Section [3.1](#) along with the FPMA light curves, binned to a resolution of 500 s. This illustrates that the *NuSTAR* observations coincide with superorbital minimum and maximum.

Using the ephemeris defined in Pearlman et al. ([2019](#)), we also folded the *Swift* BAT light curve on the 6.7828 ± 0.0004 day orbital period (see Figure [4](#)(b)). The *NuSTAR* FPMA superorbital minimum and maximum light curves are overplotted in red. This shows that the *NuSTAR* observations are clearly outside of eclipse.

To determine the neutron star rotation period in both *NuSTAR* observations, we used the epoch folding technique presented in Leahy ([1987](#)) applied to the combined FPMA +FPMB light curves binned to a resolution of 1 s. We estimated the uncertainty on the pulse period at the 1σ confidence interval by simulating 2000 light curves based on
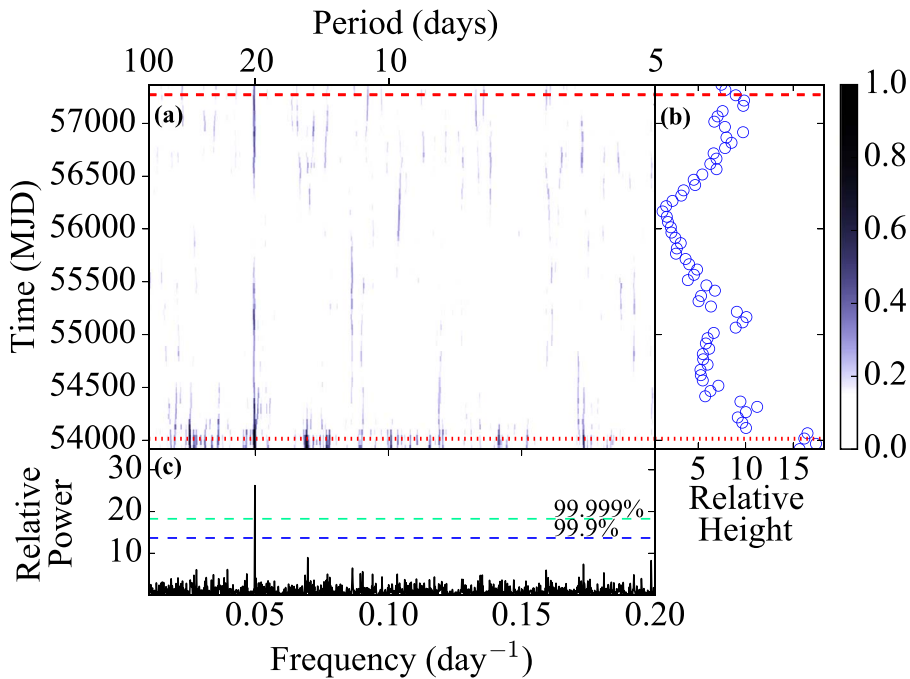
Figure 2. (a) *Swift* BAT dynamic power spectrum in the 15–50 keV band of IGR J16493-4348 as a function of time. The power spectra were calculated using 1000 day time intervals, with 50 day increments in the start and end times. The superorbital cycle coinciding with the times of the *NuSTAR* observations near superorbital minimum and maximum is indicated by the red dashed line. The *Suzaku* observation reported in Morris et al. (2009) is indicated by the dotted red line. (b) Relative height of the peak near the ∼20.06 day superorbital period in the power spectrum for each 1000 day time interval. (c) Discrete Fourier transform of the entire data set produced, with 99.9% and 99.999% significance levels indicated by the blue and green dashed lines, respectively.

the previously determined pulse period and profile with additional Poisson noise. We find the neutron star rotation period at superorbital minimum and maximum to be 1092.9 ± 0.2 s and 1092.6 ± 0.3 s, after correcting for the binary orbital motion. The neutron star rotation period shows no significant change between superorbital minimum and maximum. To investigate changes in the neutron star rotation period between our *NuSTAR* observations and the spin period reported in Pearlman et al. (2019), we calculated the Taylor expansion (see Equation (1)),

$$P(t) = P(t_0) + (t - t_0)\dot{P}, \quad (1)$$

where $P(t)$ is the neutron star rotation period derived at superorbital minimum, $P(t_0)$ is the neutron star rotation period derived in Pearlman et al. (2019), and the epoch t_0 is the maximum delay time from the pulsar timing analysis (Pearlman et al. 2019). We find the pulse period derivative between the *RXTE* observations reported in Pearlman et al. and our *NuSTAR* observation at superorbital minimum to be $(-1.8 \pm 1.7) \times 10^{-9}$ s s^{-1}, which is consistent with zero.

In Figure 5(a), we show the *NuSTAR* FPMA light curves near superorbital minimum and maximum binned to a time resolution chosen to be the mean pulse period (∼1092.7 s). We divided the light curves into two energy bands, where the soft band is defined between energies 3–10 keV and characterized by the count rate $C_{\rm soft}$, and the hard band is between 15–50 keV and denoted by the count rate $C_{\rm hard}$. We define the hardness ratios as

$$\text{HR} = \frac{(C_{\rm hard} - C_{\rm soft})}{(C_{\rm hard} + C_{\rm soft})}, \quad (2)$$

where a soft spectrum is indicated by negative values and a hard spectrum is indicated by positive values (see Figure 5(b)).

While the X-ray flux significantly increases between superorbital minimum and maximum, no change in the hardness ratio between superorbital minimum and maximum was found.

We folded the *NuSTAR* 3–50 keV light curves at superorbital minimum and maximum on the ∼1092.9 s and ∼1092.6 s periods, respectively. For the observation at superorbital maximum, we defined phase zero at the time of maximum delay (see Section 1). We aligned the pulse profiles at superorbital minimum and maximum by calculating the maximum value of the cross-correlation function between the two pulse profiles (see Figure 6). The pulse profiles at superorbital minimum and maximum each show a double-peaked structure with a main broad peak and a smaller secondary peak.

To investigate the energy dependence of the pulse profile, we divided the light curve into five energy bands defined between energies of 3–6 keV, 6–10 keV, 10–20 keV, 20–30 keV, and 30–50 keV. The pulse profiles at both superorbital minimum and maximum show a weak energy dependence (see Figure 6). Only small changes in the pulse profiles are seen, where the main peak is broad up to 20 keV and progressively becomes narrower up to ∼50 keV (see Figures 6(b)–(f)).

We define the peak-to-peak pulse fraction as

$$\mathcal{P} = \frac{(F_{\rm max} - F_{\rm min})}{(F_{\rm max} + F_{\rm min})} \quad (3)$$

where the maximum and minimum count rates in the pulse profile are characterized as $F_{\rm max}$ and $F_{\rm min}$, respectively. Using Equation (3), we found that the peak-to-peak pulsed fraction at both superorbital minimum and maximum increases with increasing energy (see Figure 7).
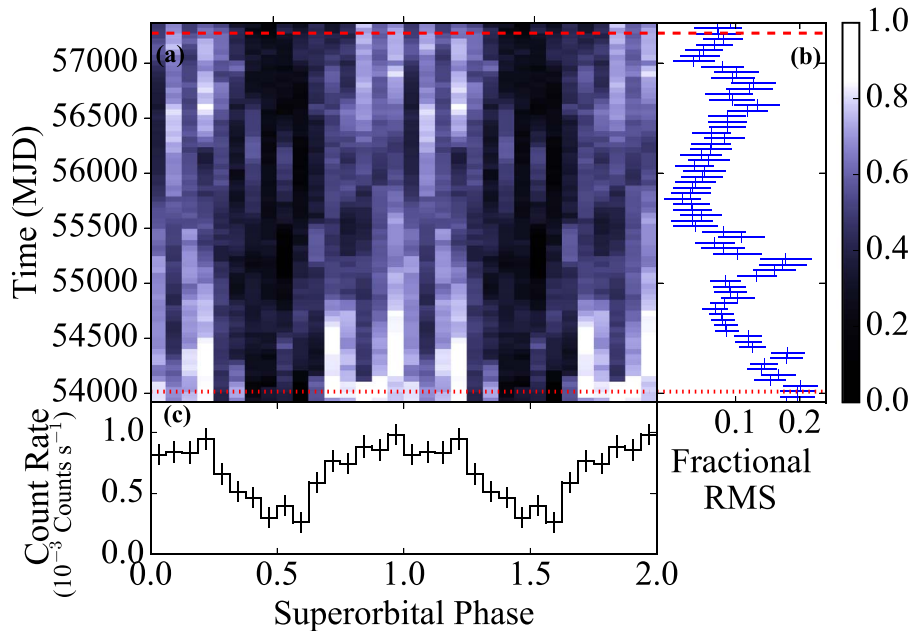
Figure 3. (a) *Swift* BAT light curve folded on the ∼20.06 day superorbital period using 16 bins as a function of time (see the text for details). (b) Variation in the fractional root mean square (rms) amplitude of the modulation as a function of time. The dynamic folded light curves and fractional rms were calculated for 1000 day time intervals, with 50 day increments in the start and end times. The superorbital cycle coinciding with the times of the *NuSTAR* observations is indicated by the short red dashed line. The *Suzaku* observation reported on in Morris et al. (2009) is indicated by the dotted red line. (c) *Swift* BAT light curve folded on the ∼20.06 day superorbital period using 16 bins.

3.3. Phase-averaged Spectral Analysis

The nearly simultaneous *NuSTAR* and *Swift* XRT spectra of IGR J16493-4348 were analyzed using the package XSPEC v12.9.1. We made use of the XSPEC convolution model cflux to calculate the fluxes and associated errors. The FPMA and FPMB spectra were simultaneously fit in XSPEC. To account for instrumental calibration uncertainties, we used cross-calibration constants normalized to FPMA during the spectral analysis (see Table 2).

To monitor the spectral evolution of the broadband X-ray emission as a function of superorbital phase, we extracted nearly simultaneous *NuSTAR* and *Swift* XRT spectra at superorbital minimum and maximum, respectively (see Figures 8(a) and (e)). For both data sets, we used several models that typically describe systems that host a neutron star: a power law (power), a power law with a high-energy cutoff (highecut; White et al. 1983), a cutoff power-law (cutoffpl), a power law with a Fermi–Dirac cutoff (fdcut; Tanaka 1986), and a negative–positive exponential cutoff (npex; Makishima et al. 1999). All models were modified by an absorber that fully covers the source (tbabs in XSPEC) using the Verner et al. (1996) cross sections and Wilms et al. (2000) abundances. We note that D'Aì et al. (2011) applied the npex, cutoffpl and fdcut models to a broadband analysis using *Swift* BAT and *INTEGRAL* ISGRI data, together with pointed *Swift* XRT and *Suzaku* observations, and found the spectra to be best described by the npex model. For our *NuSTAR* and *Swift* observations, we could not constrain the cutoff energy with the fdcut model, and found an upper limit at the 90% confidence interval of <3 keV at both superorbital minimum and maximum.

We compared the highecut, npex, and cutoffpl residuals at superorbital minimum and maximum in Figures 8(b)–(d) and (f)–(h), respectively, and found that all three models provided a similar quality of fit at superorbital

minimum (see Figure 8(a)). The highecut and npex models provided a similar quality of fit at superorbital maximum, but the cutoffpl model yielded a worse χ^2 value and wavy residuals (see Figure 8(h)). The results are given in Table 2. We note that for a power law modified by a high-energy cutoff, sharp features can appear as line-like residuals at the cutoff energy. No evidence of such line-like residuals near the cutoff energy was found in either observation (see Figure 8). Unless otherwise noted, we chose to model the spectra using the highecut model since it provided a marginally better fit quality at both superorbital minimum and maximum (see Figures 8(b) and (f)).

The neutral hydrogen column density for the fully covered absorption at superorbital minimum and maximum were found to be $(9 \pm 2) \times 10^{22}$ cm^{-2} and $(11 \pm 1) \times 10^{22}$ cm^{-2}, respectively. These measurements exceed the values reported by the Leiden/Argentine/Bonn survey (Kalberla et al. 2005) and the review by Dickey & Lockman (1990), which are 1.42×10^{22} cm^{-2} and 1.82×10^{22} cm^{-2}, respectively. This is consistent with absorbing material intrinsic to the source, which is expected for the subclass of obscured SGXBs (Chaty 2011).

Apart from the overall flux change, we find no significant changes in the continuum parameters between superorbital minimum and maximum (see Table 2). Not surprisingly, the unabsorbed X-ray flux is found to increase by more than a factor of 2, where it is found to be $(2.9 \pm 0.3) \times 10^{-11}$ erg cm^{-2} s^{-1} in the 1–10 keV band near superorbital minimum and $(7.6 \pm 0.2) \times 10^{-11}$ erg cm^{-2} s^{-1} in the 1–10 keV band near superorbital maximum. Assuming a distance of 16.1 ± 1.5 kpc (Pearlman et al. 2019), the 1–10 keV X-ray luminosity is found to be $(9 \pm 2) \times 10^{35}$ erg s^{-1} and $(2.4 \pm 0.5) \times 10^{36}$ erg s^{-1} at superorbital minimum and maximum, respectively.

To study the broadband behavior of IGR J16493-4348, we additionally calculated the unabsorbed X-ray flux and luminosity in the 3–40 keV band. At superorbital minimum, the
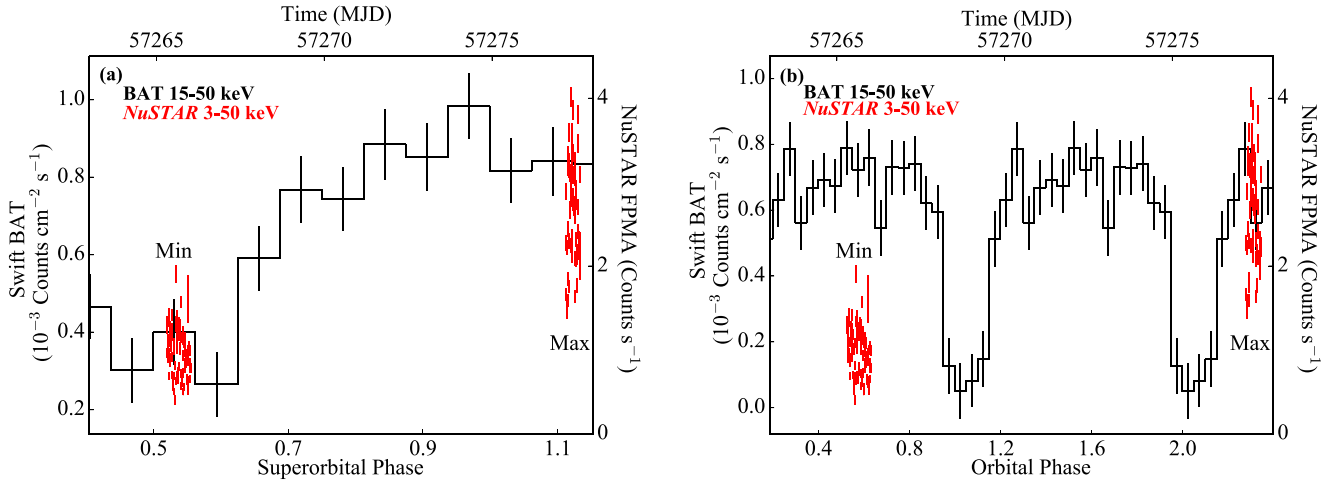
Figure 4. (a) *Swift* BAT light curve (black) folded on the ~20.06 day superorbital period using 16 bins. (b) *Swift* BAT light curve (black) folded on the ~6.7828 day orbital period using 20 bins. Phase zero for the superorbital and orbital light curves corresponds to the times of maximum flux (see Section 3.1) and maximum delay from the pulsar timing analysis in Pearlman et al. (2019), respectively. The *NuSTAR* FPMA data near superorbital minimum and maximum are overplotted in red.
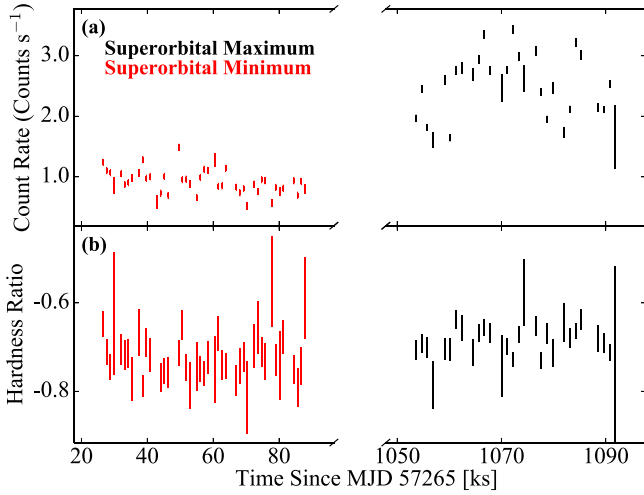

Figure 5. (a) *NuSTAR* FPMA 3–50 keV light curves and (b) hardness ratio (see the text for details) at superorbital minimum (red) and maximum (black) binned to a time resolution corresponding to the average neutron star rotation period (~1092.7 s).
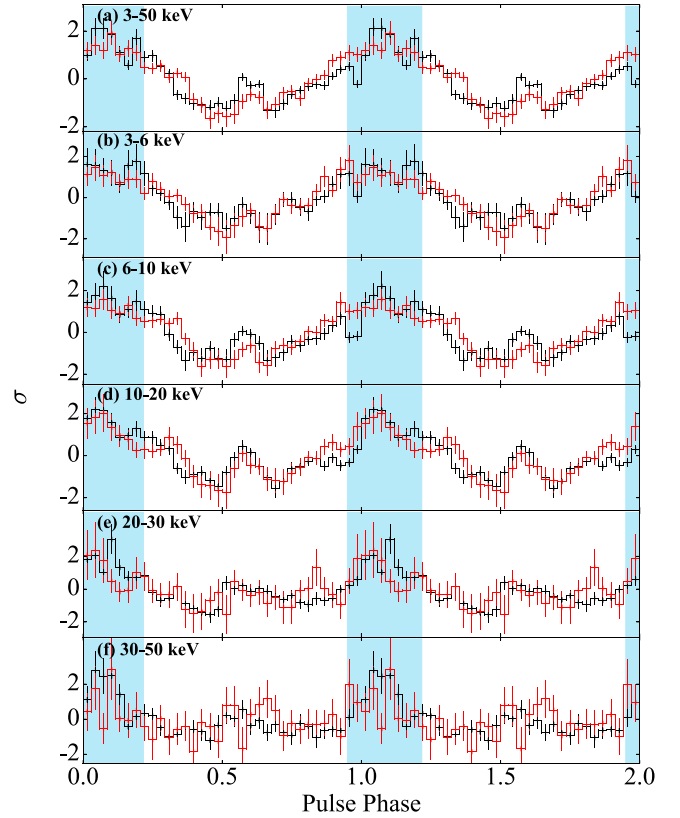

Figure 6. Energy-resolved *NuSTAR* pulse profiles at superorbital minimum (red) and superorbital maximum (black). The pulse profiles are normalized such that their mean value is zero and their standard deviation is unity. The modulation appears to be double-peaked, with a main broad peak and secondary peak offset by ~0.5 in phase. The phase range used for the pulse-peak spectral analysis is indicated by the light blue shaded region (see Section 3.5).

3–40 keV X-ray flux and luminosity were found to be $(4.9 \pm 0.2) \times 10^{-11}$ erg cm^{-2} s^{-1} and $(1.5 \pm 0.3) \times 10^{36}$ erg s^{-1}, respectively. The corresponding X-ray flux and luminosity at superorbital maximum were $(1.41 \pm 0.03) \times 10^{-10}$ erg cm^{-2} s^{-1} and $(4.4 \pm 0.8) \times 10^{36}$ erg s^{-1}, respectively.

Some residuals were found near 6.4 keV at superorbital maximum, which could indicate a weak Fe Kα emission feature (see Figure 9). We account for this with a narrow additive Gaussian with a line width fixed to 0.1 keV, as the line width was unconstrained by the fit. We also tried freezing the width of the Fe Kα line to 0.01 keV and 10^{-3} keV, but note that it did not significantly affect the best-fit continuum parameters and their uncertainties. This is not surprising since these line widths are smaller than *NuSTAR*'s FWHM energy resolution, which is 400 eV at 6.0 keV (Harrison et al. 2013).

The addition of an Fe Kα line reduces the χ^2/dof from 807.27/755 to 791.14/753. To estimate the significance of the inclusion of an Fe Kα feature to the *NuSTAR* and *Swift* spectra, we simulated 10^4 spectra using a Monte Carlo analysis (Protassov et al. 2002). The simulated spectra were modeled without the Fe Kα emission

component and were fit both with and without the additional component. We compared the difference in simulated χ^2 with the observed one, which was found to be 16.1. We found the significance of an Fe Kα feature to be 99.99%, which supports the presence of a neutral Fe Kα feature. We found its centroid energy, equivalent width, and flux are $6.36^{+0.09}_{-0.10}$ keV, 51^{+22}_{-19} eV, and $(3^{+1}_{-2}) \times 10^{-13}$ erg cm^{-2} s^{-1}, respectively (see Table 2).
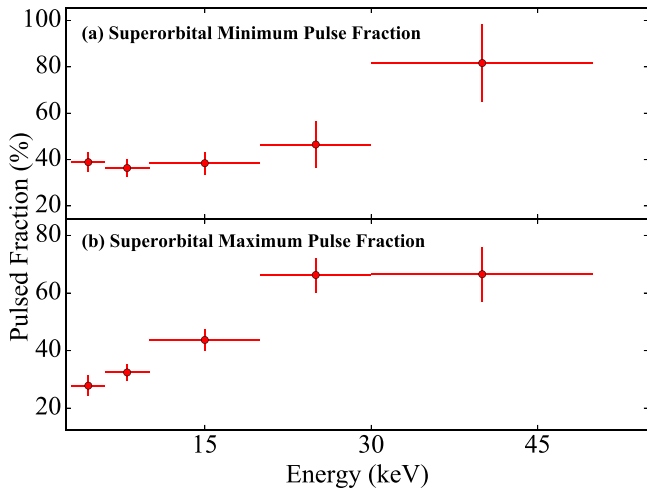
Figure 7. Energy dependence of the pulse fraction of IGR J16493-4348 observed near (a) superorbital minimum and (b) superorbital maximum.

At superorbital minimum, we found the addition of an Fe Kα feature does not significantly improve the fit quality (χ^2/dof changes from 596.17/581 to 596.12/580). Using a similar Monte Carlo analysis, we determined the significance of an Fe Kα feature to be less than 68% with 10^4 trials. From a spectral analysis using *Suzaku* and *Swift* BAT observations, Morris et al. (2009) found no evidence of strong Fe Kα features and calculated the upper limit of the equivalent width of a 6.4 keV line to be 84 eV. To fit the spectrum with the same model in both observations, we chose to include the Fe Kα line where the energy and width were fixed to the best-fit values found at superorbital maximum. We found an upper limit of 44 eV and 8.0×10^{-14} erg cm^{-2} s^{-1} at the 90% confidence interval for the equivalent width and flux of the Fe Kα line, respectively (see Table 2).

Negative residuals were found near ~20 keV at superorbital minimum, indicating the possible presence of a narrow absorption feature (see Figure 8(b)). We modeled the residuals near ~20 keV using a multiplicative line model with the centroid energy, line width, and optical depth as free parameters. We investigated the significance of a ~20 keV feature using the Monte Carlo analysis described in Protassov et al. (2002) and determined its significance to be less than ~60% with 10^4 trials, which indicates the improvement from adding an absorption component near ~20 keV is negligible. We did not find broad residuals between 30 keV and 40 keV in the *NuSTAR* spectra, even though such residuals were significant in the BAT and ISGRI spectra reported in D'Aì et al. (2011).

3.4. Pulse-phase-resolved Spectral Analysis

We investigated variations in the spectral continuum at different rotational phases of the neutron star using pulse-phase-resolved spectroscopy. Since the exposure times of the *Swift* snapshot observations were short in comparison to the *NuSTAR* observations (see Table 1), we only considered the *NuSTAR* spectra for the analysis of phase-dependent changes in the spectral parameters. For the phase-resolved analysis, we chose to subdivide the folded light curves at superorbital minimum and maximum into four equally spaced intervals. We rebinned the phase-resolved spectra using the same procedure as for the phase-averaged spectra (see Section 2.1).

We initially allowed the continuum spectral components described in Table 2 to be free parameters and performed spectral fits on each of the four equally spaced intervals. Since the phase-resolved spectra lack the soft energy coverage made available by *Swift* XRT, we chose to fix N_H to the phase-averaged values of 9×10^{22} cm^{-2} and 11×10^{22} cm^{-2} from the superorbital minimum and maximum spectra, respectively (see Table 2). We also tried to fit the data leaving the fully covered N_H free, but this resulted in large uncertainties in the model parameters.

Figure 10 shows the spectral parameters of the `highecut` model at different rotational phases of the neutron star. We find possible evidence of an increase in the folding energy between superorbital minimum and maximum near the main peak of the pulse profile (see Figure 10(d)).

In Figure 11, we show the 3σ confidence contours between the folding energy and the photon index at both superorbital minimum and maximum at each neutron star rotation period phase bin. The folding energy and photon index are found to be roughly correlated with each other. We found the folding energy significantly increases between superorbital minimum and maximum near the main peak of the pulse profile (see Figure 11(a)–(b)), confirming our results in Figure 10(d).

To investigate possible changes in the pulse-phase-resolved spectral shape between superorbital minimum and maximum, we calculated the hardness ratio using Equation (2). We defined the soft and hard bands to be 3–10 keV and 15–40 keV, respectively. The hardness ratio at the main peak of the pulse profile increases with increasing X-ray luminosity (see Figure 10(b)).

Due to the reduced signal-to-noise compared to the phase-averaged spectrum, the addition of a 6.4 keV emission feature does not significantly improve the quality of the fit in most phase intervals of the phase-resolved spectra at superorbital maximum, even though it was observed at the 99.99% confidence interval in the superorbital maximum phase-averaged spectrum (see Section 3.3). We note the Fe Kα line is significant at the 98.8% confidence intervals between pulse phases 0.75–1.00 using a Monte Carlo analysis with 10^4 trials. Since the Fe Kα line is detected in the phase-averaged spectrum at superorbital maximum, we chose to include it in our pulse-phase-resolved spectra at both superorbital maximum and superorbital minimum with the centroid energy and width frozen to the value determined from the phase-averaged spectrum at superorbital maximum. No fluctuations in the flux of the Fe Kα line as a function of neutron star rotation period were found (see Figure 10(f)), which could possibly be attributed to the low signal to noise.

3.5. Pulse-peak Spectral Analysis

To further investigate possible spectral differences between superorbital minimum and maximum near the broad main peak of the pulse profile, we extracted a spectrum for each observation focusing on pulse phases 0.00–0.22 and 0.88–1.00. We rebinned the pulse-peak-resolved spectra using the same procedure as for the phase-averaged and phase-resolved spectra and again only considered the *NuSTAR* spectra for the analysis.

For the pulse-peak spectral analysis, we fit the spectra at both superorbital minimum and maximum simultaneously using the procedure described in Kühnel et al. (2016 and references therein). To reduce the number of free parameters, we froze the

Table 2
Phase-averaged, Broadband X-Ray Spectral Parameters of the Nearly Simultaneous *NuSTAR* and *Swift* Observations for Several Empirical Models

Model Parameter	Highecut		NPEX		CutoffPL	
	Superorbital Minimum	Superorbital Maximum	Superorbital Minimum	Superorbital Maximum	Superorbital Minimum	Superorbital Maximum
χ_ν^2 (dof)	1.03 (581)	1.05 (753)	1.04 (580)	1.08 (753)	1.06 (581)	1.13 (754)
C_{FPMA}[a]	1	1	1	1	1	1
C_{FPMB}[a]	1.03 ± 0.02	1.03 ± 0.01	1.03 ± 0.02	1.03 ± 0.01	1.03 ± 0.02	1.03 ± 0.01
C_{XRT}[a]	0.9 ± 0.2	0.80 ± 0.07	0.9 ± 0.2	0.80 ± 0.07	0.9 ± 0.2	0.80 ± 0.07
Cutoff energy (keV)	$6.9^{+1.3}_{-0.7}$	$8.1^{+0.4}_{-0.5}$	...	...	...	...
Folding energy (keV)	15^{+3}_{-2}	19 ± 2	8^{+2}_{-1}	$8.7^{+1.1}_{-0.9}$	12^{+2}_{-1}	14 ± 1
$Norm_n$ ($\times 10^{-4}$)	...	...	$0.9^{+1.6}_{-0.7}$	$0.9^{+0.7}_{-0.5}$	...	...
Tbabs N_H ($\times 10^{22}$ cm^{-2})	9 ± 2	11 ± 1	9^{+2}_{-1}	10 ± 1	10 ± 2	11 ± 1
Γ	1.3 ± 0.2	$1.31^{+0.07}_{-0.08}$	$0.7^{+0.2}_{-0.1}$	$0.72^{+0.10}_{-0.09}$	1.0 ± 0.1	0.99 ± 0.09
Normalization ($\times 10^{-2}$)	$0.36^{+0.17}_{-0.09}$	$0.9^{+0.2}_{-0.1}$	$0.29^{+0.07}_{-0.05}$	$0.65^{+0.09}_{-0.08}$	$0.39^{+0.09}_{-0.07}$	0.8 ± 0.1
Fe Kα energy (keV)	6.36[b]	$6.36^{+0.09}_{-0.10}$	6.4[b]	6.4 ± 0.1	6.4[b]	6.4 ± 0.1
Fe Kα width ($\sigma_{Fe\,K\alpha}$)[c]	0.1	0.1	0.1	0.1	0.1	0.1
Normalization ($\times 10^{-3}$ photons cm^{-2} s^{-1})	<0.01	0.04 ± 0.02	<0.01	0.04 ± 0.02	<0.01	0.04 ± 0.02
Fe Kα EW (eV)	<44	51^{+22}_{-19}	<44	44^{+32}_{-18}	<44	47^{+21}_{-19}
Fe Kα Flux ($\times 10^{-13}$ erg cm^{-2} s^{-1})	<0.8	3^{+1}_{-2}	<1.0	$2.5^{+0.9}_{-1.8}$	<0.7	$3^{+1}_{-2.9}$
Absorbed flux ($\times 10^{-11}$ erg cm^{-2} s^{-1})[d]	1.98 ± 0.03	4.90 ± 0.06	1.96 ± 0.03	4.87 ± 0.05	1.95 ± 0.03	4.85 ± 0.05
Unabsorbed flux ($\times 10^{-11}$ erg cm^{-2} s^{-1})[e]	2.9 ± 0.3	7.6 ± 0.2	$2.9^{+0.2}_{-0.1}$	7.3 ± 0.3	3.1 ± 0.2	7.7 ± 0.3

Notes.
[a] Detector cross-calibration constants with respect to FPMA.
[b] The energy is frozen because we can only obtain an upper limit.
[c] The width of the Fe Kα line is frozen to 0.1 keV.
[d] Absorbed flux in the 1–10 keV band.
[e] Unabsorbed flux in the 1–10 keV band.

energy and width of the Fe Kα feature to the phase-averaged value at superorbital maximum. Again, the Fe Kα feature was not detected at superorbital minimum and we therefore derived an upper limit for the strength of the line.

In Figure 12, we show the pulse-peak *NuSTAR* FPMA spectra and count rate ratio at superorbital minimum and maximum. At energies above 10 keV, we find possible evidence of a harder spectrum at superorbital maximum than at superorbital minimum (see Figure 12(b)). This is consistent with the increase in the hardness ratio from superorbital minimum to superorbital maximum near the peak of the pulse profile (see Figure 10(b)). To investigate changes in the shape of the spectrum between superorbital minimum and maximum, we first fit the pulse-peak spectra at both superorbital phases simultaneously and only allowed the cross-normalization for each spectrum to change. In these fits, the continuum parameters were all tied together to have the same value for the superorbital minimum and maximum spectra (see Brumback et al. 2018 and references therein). We find χ_ν^2 to be 1.14 for 838 dof, 1.15 for 838 dof and 1.18 for 837 dof for the highecut, npex, and cutoffpl models, respectively. The cutoff energy, folding energy and photon index for the highecut model were found to be 8.0 ± 0.3 keV, 22 ± 1 keV, and 1.35 ± 0.03, respectively.

We also fit the pulse-peak spectra at superorbital minimum and maximum, where the folding energy was allowed to vary. This reduces the χ_ν^2 for the highecut, npex, and cutoffpl models to 1.01 for 836 dof, 1.02 for 836 dof, and 1.05 for 835 dof, respectively (see Table 3). The folding energy for the highecut and cutoffpl models shows a

possible increase between superorbital minimum and maximum, which is consistent with our pulse-phase-resolved results (see Figure 10(b)).

We detected possible negative residuals near ~22 keV in the pulse-peak spectrum at superorbital minimum (see Figure 13(a)). To investigate the possibility of an absorption feature, we only fit the pulse-peak spectrum at superorbital minimum and accounted for the residuals with a multiplicative Gaussian absorption feature. The addition of an absorption line reduces the χ^2/dof for the highecut model from 324.69/314 to 314.82/312 (see Figures 13(b) and (c)). We note the width of the feature cannot be constrained and instead we find the upper limit of the width to be 0.4 keV. The energy and optical depth of the possible absorption feature for the highecut model are found to be 23.1 ± 0.4 keV and $0.8^{+0.4}_{-0.2}$, respectively. We do not find a significant change in the spectral parameters if instead we use a Lorentzian optical depth profile to describe the possible absorption line. In this case, the χ^2/dof for the highecut model is reduced from 324.69/314 to 315.07/312.

We also investigated the possibility that the choice of the continuum influences the energy and shape of the possible absorption feature. For the npex and cutoffpl models, the addition of an absorption line reduces the χ^2/dof from 330.15/314 to 319.91/312 and 338.40/315 to 329.17/313, respectively (see Figures 13(d)–(g)). The energy of the line is found to be 23.3 ± 0.4 keV and 23.3 ± 0.5 keV for the npex and cutoffpl models, respectively.

To determine the significance of the inclusion of the possible absorption feature, we simulated 10^4 spectra using the Monte Carlo analysis described in Protassov et al. (2002). Unlike our
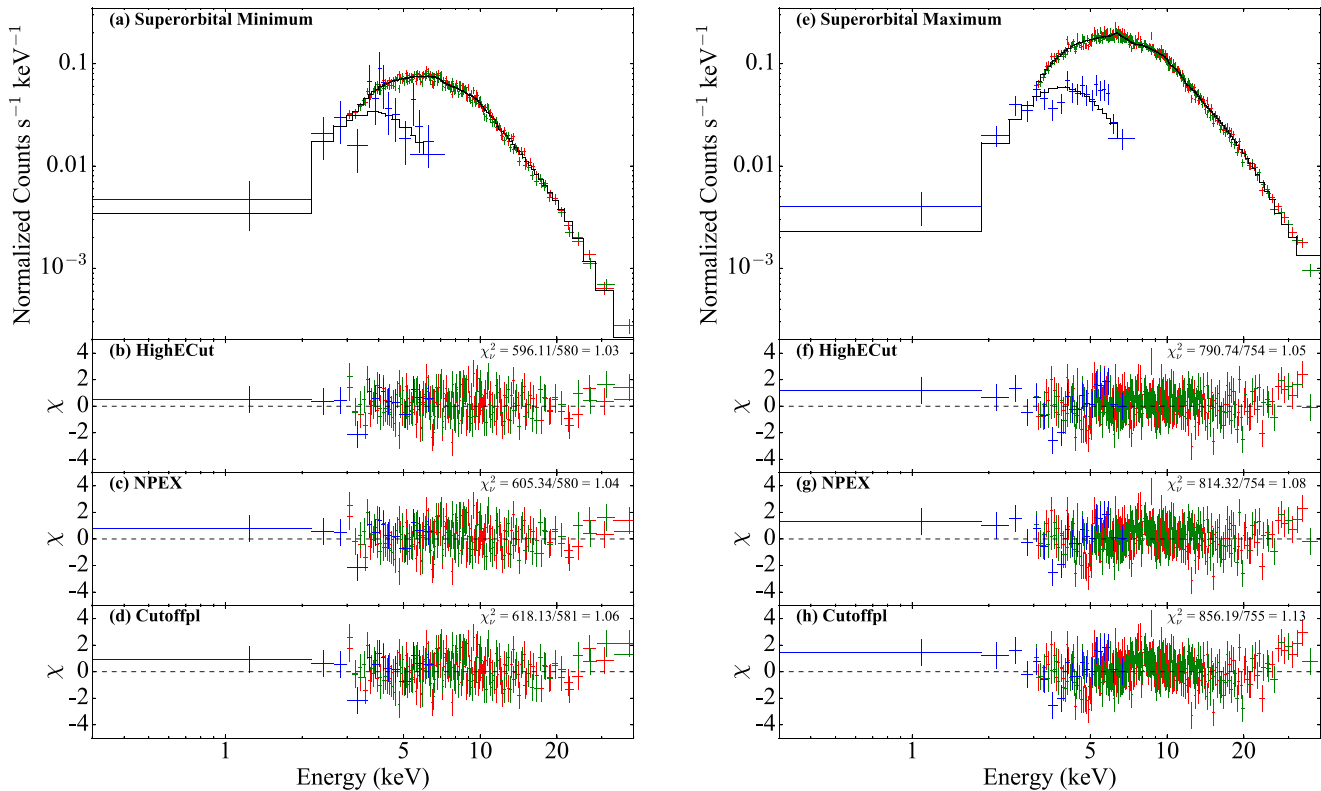
Figure 8. Broadband *NuSTAR+Swift* spectra of IGR J16493-4348 at (a) superorbital minimum and (e) superorbital maximum where the FPMA, FPMB, and XRT data are shown in red, green, and blue, respectively. The best-fit `highecut` model is shown in black. Both models consist of a continuum comprised of an absorbed power law with a high-energy cutoff and an emission line near 6.4 keV. Residuals of the best-fit `highecut` model are plotted for (b) superorbital minimum and (f) superorbital maximum, respectively. Residuals for the `NPEX` model are plotted for (c) superorbital minimum and (g) superorbital maximum, respectively. Residuals for the `cutoffpl` model are plotted for (d) superorbital minimum and (h) superorbital maximum, respectively. The spectra are rebinned for clarity.

Monte Carlo simulations for Fe Kα where we restricted the energy to that of the best-fit model (see Sections 3.3 and 3.4), we allowed the energy of the possible absorption feature to vary between 10 keV and 40 keV. These are reasonable values for a possible CRSF (Coburn et al. 2002). We determined the probability of the possible absorption feature arising by chance to be 36.4% with 10^4 trials, which shows that the feature is not significant.

4. Discussion

4.1. Spectral Evolution as a Function of Superorbital Period

In Figure 14, we plot the photon index and folding energy of the pulse-phase-averaged *NuSTAR* and *Swift* XRT data as a function of the 1–10 keV X-ray luminosity. For the `highecut` model, the pulse-phase-averaged X-ray luminosity of IGR J16493-4348 increased from $(9 \pm 2) \times 10^{35}$ erg s^{-1} at superorbital minimum to $(2.4 \pm 0.4) \times 10^{36}$ erg s^{-1} at superorbital maximum (see Section 3.3). To place the data in context, we also show the change in the photon index and folding energy with respect to 1–10 keV X-ray luminosity of the broadband *Swift* BAT and the *INTEGRAL* ISGRI, together with pointed *Swift* XRT and *Suzaku* observations reported in D'Aì et al. (2011). The *Swift* XRT and *Suzaku* observations of IGR J16493-4348 took place at MJD 53,805.9–53,806.4 and MJD 54,013.9–54,014.4, respectively; which correspond to superorbital phases ~0.05–0.07 and ~0.42–0.45 or slightly earlier superorbital phases than our *NuSTAR* campaign. Their X-ray luminosities, however, are similar to our *NuSTAR* observations (see Figure 14).

In accreting X-ray pulsars, the shape of the pulse profiles has been found to depend on the emission processes and the relative contribution of the two accretion columns (Meszaros & Nagel 1985; Kraus et al. 1989; Falkner et al. 2019). Our *NuSTAR* observations of IGR J16493-4348 show that, despite the increase in X-ray flux, the pulse profiles show no significant changes in shape between superorbital minimum and maximum. The pulse profiles in both observations were found to weakly depend on energy and be double-peaked in structure (see Figure 6). This may indicate that the emission properties in the accretion column may not change between the two superorbital phases (e.g., A 0535+26; Ballhausen et al. 2017). Using *RXTE* PCA data that span times between MJD 55,843.1 and MJD 55,852.6, corresponding to superorbital phases 0.62–0.09, Pearlman et al. (2019) also found a double-peaked shape of the pulse profiles and a weak energy dependence. They also observed the pulsed fraction to increase with increasing energy, which we confirm with *NuSTAR* (see Figure 7). We suggest the similar properties of pulse profiles as seen by both *NuSTAR* and *RXTE* may be linked to an accretion regime that does not change between superorbital minimum and maximum (see Postnov et al. 2015 and references therein).

In X-ray binaries that host accretion powered pulsars, the physical conditions inside the accretion column depend on the mass accretion rate. The resulting X-ray emission can be characterized in terms of the local Eddington limit ($L_{\rm crit}$, Becker et al. 2012), which for a magnetic dipole geometry is proportional to the magnetic field strength. As indicated in Section 1, the magnetic field of the neutron star is often directly measured by CRSFs. We do not find any significant CRSFs in
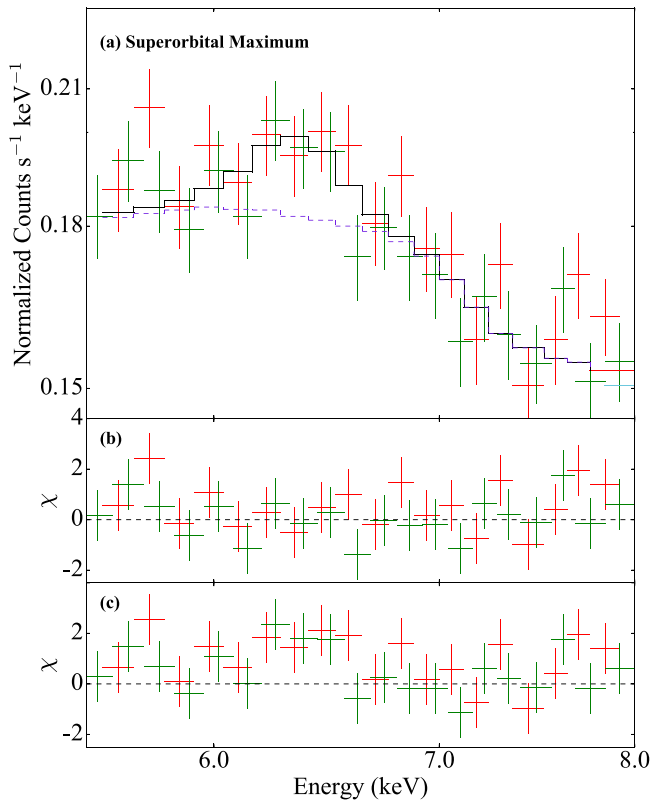
Figure 9. FPMA+FPMB spectrum of IGR J16493-4348 between 5.5-8.0 keV band at superorbital maximum. The Fe Kα emission line is shown along with the best-fit model (black). (a) FPMA and FPMB data indicated by the red and green data points. The dashed purple line indicates the fit without the Fe Kα emission line. (b) Residuals with the Fe Kα emission line included in the spectral model. (c) Residuals without the Fe Kα emission line included in the spectral model.

Figure 10. *NuSTAR* spectral parameters as a function of pulse phase using the power law with high-energy cutoff model. The observations at superorbital minimum and maximum are indicated by the red and blue points, respectively. The gray histogram shows the *NuSTAR* light curve at superorbital maximum in the 3–50 keV energy range folded on the neutron star rotation period.

the pulse phase-averaged or phase-resolved *NuSTAR* spectra of IGR J16493-4348, which is a possible indication that the magnetic field might be predominately seen under small viewing angles (Schwarm et al. 2017).

At low to intermediate accretion rates, the X-ray luminosity is below the critical value where radiation pressure becomes important. The in-falling matter may be primarily decelerated by Coulomb interactions, and is thought to form an accretion mound close to the surface of the neutron star (Postnov et al. 2015 and references therein). Our *NuSTAR* results show that the X-ray luminosity observed in IGR J16493-4348 is on the order of 10^{35}–10^{36} erg s^{-1}, which is consistent with this picture (see Becker et al. 2012 and references therein).

The spectral shape in X-ray binary pulsars that are accreting at low to intermediate accretion rates is observed to harden toward higher X-ray fluxes (e.g., Her X-1, A 0535+26; Klochkov et al. 2011; Ballhausen et al. 2017). Our pulse-phase-resolved *NuSTAR* results of IGR J16493-4348 near the broad main peak of the pulse profile show that the pulse-phase-resolved hardness ratio increases between superorbital minimum and maximum (see Figure 10(b)), which is a possible indication that the spectrum hardens with increasing X-ray flux. This is also supported by the ratio of the two peak spectra, which shows a clear slope, indicating the increasing dominance of the flux at superorbital maximum toward higher energies (see Figure 12(b)).

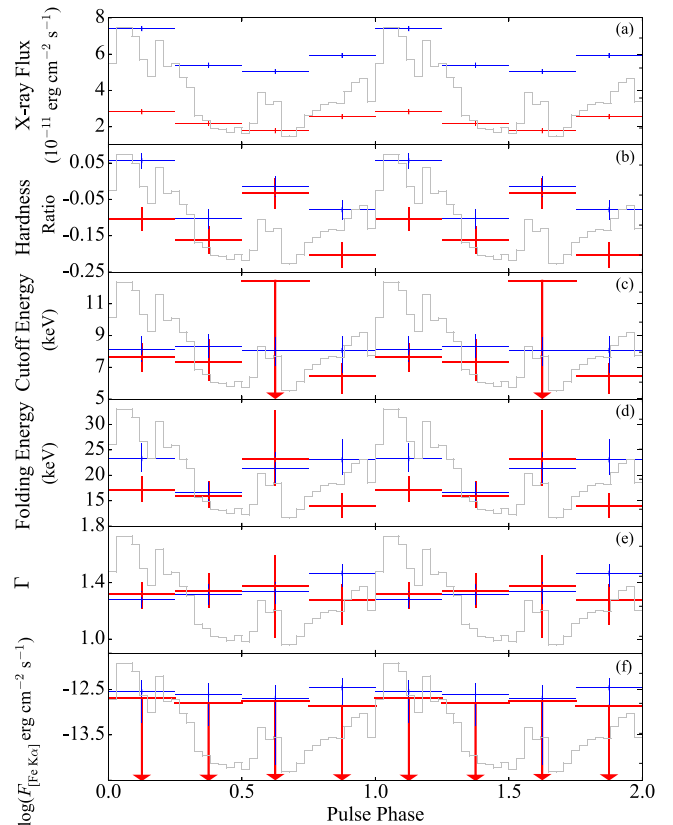It is interesting to note that D'Aì et al. (2011) found the photon index flattens between superorbital minimum and

maximum (see Figure 14(a)). While this may also suggest that the spectral shape of IGR J16493-4348 hardens with increasing X-ray flux, the photon indices observed with *NuSTAR* were found to be consistent between the superorbital minimum and maximum. As shown in Figure 14, they were additionally found to be consistent with those reported in D'Aì et al. (2011). It should also be noted that D'Aì et al. found the folding energy in their broadband BAT and ISGRI, together with pointed *Swift* XRT and *Suzaku* observations, to be systematically higher than those we derived with *NuSTAR* (see Figure 14(b)). These differences may result from the fact that the spectral shape may have changed between the observations reported in D'Aì et al. and our *NuSTAR* observations. Another possible reason is the energy gap between the soft (*Swift* XRT and *Suzaku*) and hard (*INTEGRAL* and *Swift* BAT) bands, which may affect the spectral fits reported in D'Aì et al.

This observed spectral hardening seen near the main peak of the pulse profile could possibly be explained by Compton-saturated emission from the sidewall of the optically thick accretion column (Postnov et al. 2015). We found the folding energy near the main pulse peak to increase between super-orbital minimum and maximum, but no change in the photon index was found (see Table 3). This may suggest the average temperature of the Comptonizing gas increases between superorbital minimum and maximum. Due to this temperature increase, the plasma more efficiently upscatters photons to higher energies via the inverse Compton effect, resulting in a harder observed spectrum as is observed in the pulse-peak superorbital maximum spectrum.
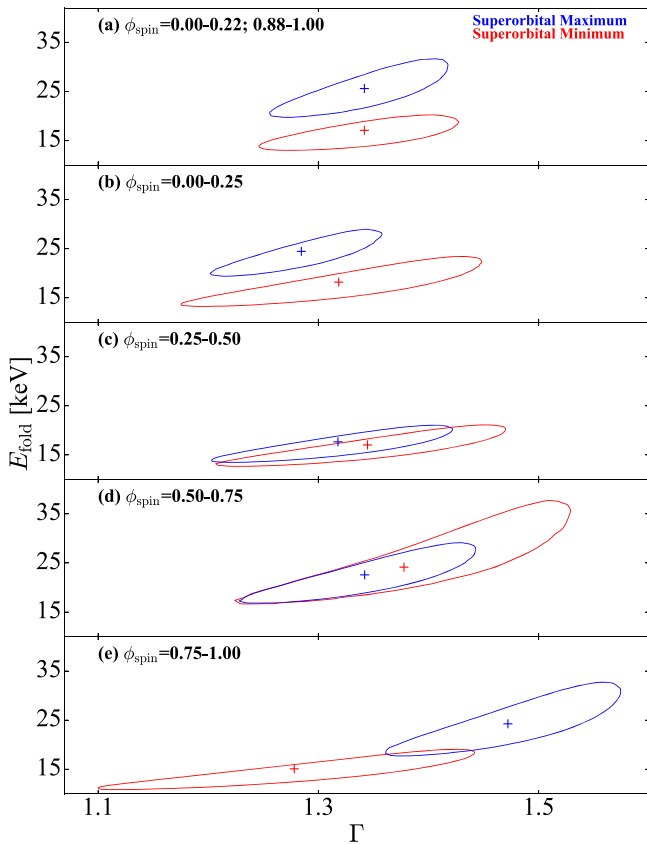
Figure 11. Contours of the folding energy, E_{fold}, and photon index, Γ, at the 3σ confidence interval for the phase-resolved spectra at superorbital minimum (red) and maximum (blue). The neutral hydrogen column density, Fe Kα energy, and detector calibration constants were held constant. The best-fit values at superorbital minimum and maximum are indicated by the red and blue crosses, respectively.
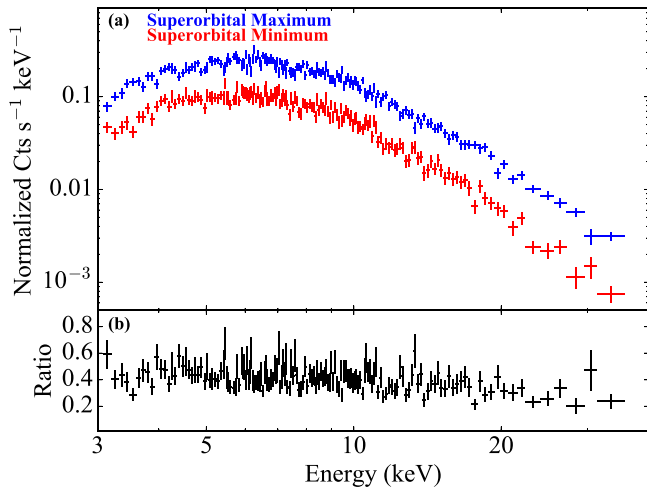

Figure 12. (a) Pulse-peak FPMA spectra at superorbital minimum (red) and superorbital maximum (blue). The superorbital maximum spectrum was rebinned to match the energy binning of the superorbital minimum spectrum for the plot to compare the residuals on a bin-by-bin basis. (b) Count rate spectral ratio between superorbital minimum and maximum (see the text for details).

4.2. Comparison with 2S 0114+650

To place IGR J16493-4348 in context with other wind-fed SGXBs where superorbital variability is found, we compare it with 2S 0114+650. This is a wind-fed SGXB where a

$\sim$30.7 day superorbital period was found (Farrell et al. 2006). The spectral type of the mass donor in 2S 0114+650 was found to be B1 I (Reig et al. 1996), which is similar to the B0.5 Ia spectral type in IGR J16493-4348 (Pearlman et al. 2019), and its distance was estimated to be 7.2 kpc.

We first discuss the *Swift* BAT observations of IGR J16493-4348 in comparison to the long-term monitoring of the 30.7 day cycle present in 2S 0114+650. Using *RXTE* All-Sky Monitor (ASM) data that spanned $\sim$8.5 yr, Farrell et al. (2006) found that the amplitude of the 30.7 day modulation changed as a function of time. This was recently confirmed by Hu et al. (2017) using ASM and BAT data spanning $\sim$20 yr. No significant changes in its frequency were found, which is similar to what we find for IGR J16493-4348.

We also discuss pointed observations of 2S 0114+650 and how they compare with our joint *NuSTAR* and *Swift* campaign for IGR J16493-4348. In their *RXTE* campaign, which covered two cycles of the $\sim$30.7 day period, Farrell et al. (2008) found no changes in the intrinsic neutral column density on superorbital timescales. The spectral shape in 2S 0114+650 was found to harden as the superorbital cycle progressed from minimum to maximum (Farrell et al. 2008), which is similar to our pulse-peak analysis of IGR J16493-4348 (see Sections 3.4–3.5). We note Farrell et al. (2008) have shown that the photon index increases by a factor of two between superorbital maximum and minimum in 2S 0114+650, which is not seen in our observations of IGR J16493-4348.

Although 2S 0114+650 and IGR J16493-4348 are both mediated by wind accretion, their superorbital modulations may show somewhat different spectral behavior. The spectrum of 2S 0114+650 significantly hardened toward higher luminosities, but the correlation between spectral hardness and X-ray luminosity in IGR J16493-4348 may be weaker and is observed only near the peak of the pulse profile (see Sections 3.4–3.5). To investigate these possible differences between 2S 0114+650 and IGR J16493-4348, we compare the accretion regimes between the two sources.

Farrell et al. (2008) found that the average absorbed 3–50 keV X-ray flux of 2S 0114+650 was 2.3×10^{-10} erg cm^{-2} s^{-1} and the fully covered absorption to be $3.2^{+0.9}_{-0.8} \times 10^{22}$ cm^{-2}. To investigate whether IGR J16493-4348 and 2S 0114+650 are accreting in similar accretion regimes, we calculated the unabsorbed X-ray luminosity in 2S 0114+650. Assuming the spectral parameters reported in Farrell et al. (2008), we corrected for absorption using PIMMS and found the unabsorbed 3–50 keV X-ray flux in 2S 0114+650 to be 2.4×10^{-10} erg cm^{-2} s^{-1}. The average 3–50 keV X-ray luminosity of 2S 0114+650 is found to be 1.5×10^{36} erg s^{-1}, which is of the same order of magnitude as the average 3–50 keV X-ray luminosity observed in IGR J16493-4348 with *NuSTAR* and *Swift* XRT (see Section 3.3). Our results near the peak of the pulse profile show that changes in the spectral shape of IGR J16493-4348 are similar to those of 2S 0114+650, albeit the trend in IGR J16493-4348 is somewhat weaker.

4.3. Superorbital Modulation in ULX Sources

Superorbital modulation on timescales of tens of days has also been detected in ULX pulsars (e.g., NGC 5907 ULX1, NGC 7793 P13, M82 X-2; Walton et al. 2016; Fürst et al. 2018; Brightman et al. 2019), accreting neutron stars with apparent luminosities in excess of 10^{39} erg s^{-1}. While such timescales are similar to those seen in X-ray binaries accreting at sub-Eddington rates, it is important to note that the timing

Table 3
Pulse-peak-resolved Broadband X-Ray Spectral Parameters

Model Parameter	Highecut		NPEX		CutoffPL	
	Superorbital Minimum	Superorbital Maximum	Superorbital Minimum	Superorbital Maximum	Superorbital Minimum	Superorbital Maximum
χ^2_ν (dof)	1.01 (836)		1.02 (836)		1.05 (835)	
C_{FPMA}	1[a]	2.44 ± 0.06[a]	1[a]	2.12 ± 0.08[a]	1[a]	2.13 ± 0.09[a]
C_{FPMB}	1.03 ± 0.02[a]	2.51 ± 0.06[a]	1.03 ± 0.02[a]	$2.18^{+0.09}_{-0.08}$[a]	1.03 ± 0.02[a]	2.19 ± 0.09[a]
Cutoff energy (keV)	$7.7^{+0.7}_{-0.9}$		...	...	...	...
Folding energy (keV)	16 ± 1	24 ± 3	$8.2^{+1.2}_{-0.9}$	10^{+2}_{-1}	13 ± 1	18 ± 2
$Norm_n$ ($\times 10^{-4}$)	...	...		$0.8^{+0.8}_{-0.4}$	...	...
Tbabs N_H ($\times 10^{22}$ cm^{-2})[b]	9	11	9	10	10	11
Γ	$1.34^{+0.05}_{-0.07}$		$0.79^{+0.09}_{-0.08}$		1.10 ± 0.06	
Normalization ($\times 10^{-2}$)	$0.48^{+0.04}_{-0.05}$	1.2 ± 0.1	0.38 ± 0.03	$0.81^{+0.08}_{-0.07}$	0.51 ± 0.04	$1.09^{+0.10}_{-0.09}$
Fe Kα energy (keV)[b]	6.36		6.4		6.4	
Fe Kα width ($\sigma_{Fe\,K\alpha}$)[b]	0.1		0.1		0.1	
Normalization ($\times 10^{-3}$ photons cm^{-2} s^{-1})	<0.03	0.05 ± 0.03	<0.03	0.047 ± 0.005	<0.03	0.05 ± 0.02
Fe Kα EW (eV)	<66	76^{+11}_{-52}	<66	51^{+30}_{-26}	<62	57^{+24}_{-32}
Fe Kα flux ($\times 10^{-13}$ erg cm^{-2} s^{-1})	<1.9	3^{+1}_{-2}	<1.7	3 ± 2	<1.7	3^{+1}_{-2}
Absorbed flux ($\times 10^{-11}$ erg cm^{-2} s^{-1})[c]	2.33 ± 0.03	5.5 ± 0.1	2.33 ± 0.03	5.5 ± 0.1	$2.29^{+0.04}_{-0.05}$	5.5 ± 0.2
Unabsorbed flux ($\times 10^{-11}$ erg cm^{-2} s^{-1})[d]	2.87 ± 0.04	7.0 ± 0.2	2.90 ± 0.04	7.0 ± 0.2	2.94 ± 0.06	7.1 ± 0.2

Notes.
[a] Cross-normalizations between detectors are calculated with respect to the value of FPMA at superorbital minimum.
[b] The neutral hydrogen absorption column density, Fe Kα line energy and width are frozen to the phase-averaged values at superorbital maximum.
[c] Absorbed flux in the 3–10 keV band.
[d] Unabsorbed flux in the 3–10 keV band.

and spectral properties of ULXs show significant differences compared to those observed in wind-fed SGXBs such as IGR J16493-4348. Due to their super-Eddington X-ray luminosities, the mode of accretion in ULX pulsars has been ascribed to Roche-lobe overflow (Bachetti et al. 2014) and the superorbital mechanism is likely to be partially driven by a precessing accretion disk (see Fürst et al. 2017 and references therein). The modulation amplitude between superorbital minimum and maximum in ULX pulsars show similarities with X-ray binaries where superorbital variations are driven by a precessing disk. For example, the amplitude of the 60 day modulation observed in M82 X-2 was found to vary by two orders of magnitude (Brightman et al. 2019), which is similar the variability observed in LMC X-4 (Molkov et al. 2015).

Some ULX pulsars have also been observed to exhibit "off" states, where their X-ray fluxes were found to be up to several orders of magnitude lower than expected from an extrapolation of their observed periodic signals (Walton et al. 2016). While the amplitude of the superorbital modulation was found to significantly change on long timescales (see Figure 2), no evidence of "off" states was revealed in our *Swift* BAT observations in IGR J16493-4348.

4.4. Superorbital Modulation Mechanism

4.4.1. Precessing Accretion Disk

We first discuss the possibility that the ∼20 day modulation in IGR J16493-4348 is driven by a precessing accretion disk (e.g., Her X-1; Scott et al. 2000). Large variations in the intrinsic neutral hydrogen absorption column are found in this case, (e.g., Her X-1; Ramsay et al. 2002) resulting in sharp dips in the superorbital profile (e.g., Her X-1, SMC X-1; Klochkov et al. 2006; Trowbridge et al. 2007). No significant changes in

N_H are observed between superorbital minimum and maximum (see Table 2), providing evidence against this model. Dramatic changes in the strength of X-ray pulsations have also been found in sources where superorbital modulation is linked to the precession of an accretion disk such as SMC X-1 (Pike et al. 2019) and ULX pulsars (e.g., M82 X-2; Bachetti et al. 2014). In these sources, the variations in the strength of the pulsations were not accompanied by large changes in X-ray flux. No such changes in the pulse profile and pulsed fraction that can be explained by variations in absorption are observed in IGR J16493-4348, which suggests that the 20 day modulation is probably not driven by a precessing accretion disk.

If the ∼20.6 day modulation was driven by a moderately long-lived prograde transient accretion disk, long-term variations in its modulation amplitude may be observable (e.g., 2S 0114+650; Hu et al. 2017). In the BAT dynamic power spectrum, we found a low amplitude in the superorbital modulation spanning ∼600 days (see Figure 2), which is similar to the formation and dissipation timescale of a transient accretion disk proposed to be present in 2S 0114+650. We note in systems where a transient disk may be present, the neutron star is expected to rapidly spin up due to the large angular momentum transfered to it (e.g., OAO 1657-415; Jenke et al. 2012). Pearlman et al. (2019) found no evidence of a rapid spin-up torque in their pulsar timing analysis using the *RXTE* PCA, which suggests that a transient accretion disk may not be present.

4.4.2. Stellar Triple System

Next, we discuss the possible case that IGR J16493-4348 is part of a triple-star system (e.g., 4U 1820-30; Chou & Grindlay 2001). In a triple-star system, the eccentricity of the
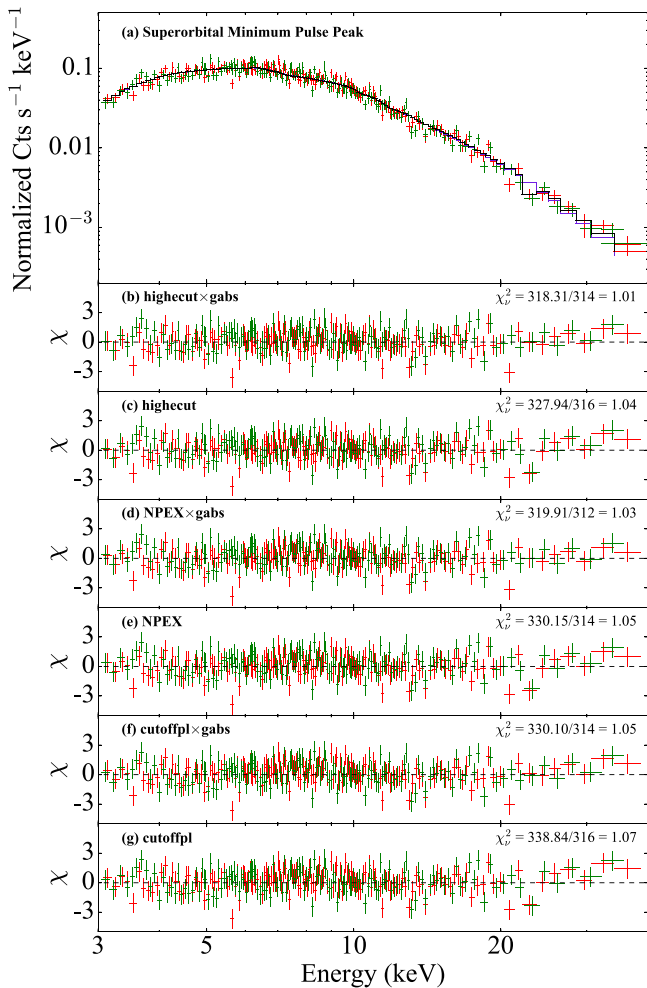
Figure 13. (a) Pulse-peak *NuSTAR* spectra of IGR J16493-4348 at superorbital minimum. The FPMA and FPMB data are shown in red and green, respectively. The `highecut` model is shown in black. (b) Residuals for the `highecut` model with the possible absorption line modeled by a Gaussian profile included in the model. (c) Residuals for the `highecut` continuum model and Fe Kα feature with no absorption line included in the model. (d) Residuals for the `npex` model with the possible absorption line modeled by a Gaussian profile included in the model. (e) Residuals with no absorption line included in the `npex` model. (f) Residuals for the `cutoffpl` model with the possible absorption line modeled by a Gaussian profile included in the model. (g) Residuals with no absorption line included in the `cutoffpl` model.

Figure 14. Evolution of the power-law (a) photon index and (b) folding energy with the 1–10 keV X-ray luminosity for the `npex` model. The *Suzaku/Swift* BAT/*INTEGRAL* ISGRI (D'Aì et al. 2011), *Suzaku/Swift* BAT/*INTEGRAL* ISGRI (D'Aì et al. 2011), and *NuSTAR* results (this work) are indicated by the green circles, red diamonds, and black crosses, respectively.

inner binary is modulated at a long-term period by tidal forces of a third companion star orbiting the center of mass between it and the inner binary (Mazeh & Shaham 1979). This period is inversely proportional to the period of the inner binary, and directly proportional to the orbital period of the third companion (see Equation (19) in Zdziarski et al. 2007). If this model is applied to IGR J16493-4348, we calculate the third period to be 11.666 ± 0.002 days. This period is only a factor of ~1.7 times larger than the binary orbital period measured with *RXTE* and *Swift* (Pearlman et al. 2019), which may imply an unstable orbital configuration if IGR J16493-4348 were part of a triple-star system.

The stability of a triple-star system depends on the ratio between the semimajor axis of the third companion star and the orbital separation of the components in the inner binary (Zdziarski et al. 2007; Mikkola 2008). Combining the ratio between the outer and inner periods with Kepler's third law, we calculate the ratio between the outer and inner semimajor axes
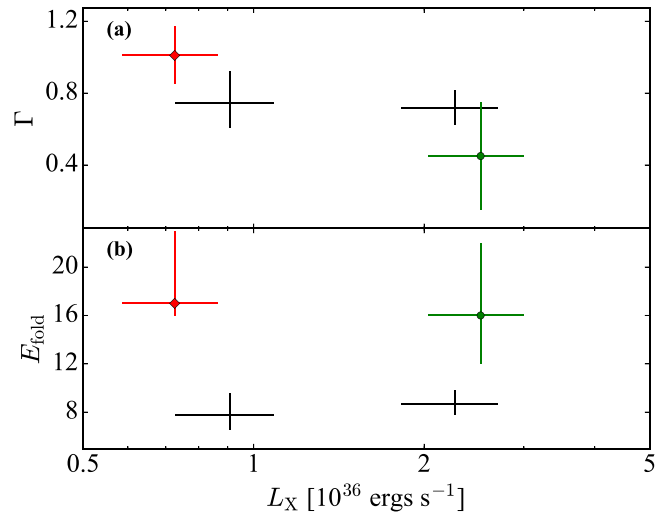
to be ~1.4. This close configuration may result in perturbations of the binary motion on timescales between the orbital period and the superorbital modulation, which were not observed with *RXTE* or *Swift* (see, e.g., Pearlman et al. 2019). It is worth noting that, depending on the mass of the third companion star, strong perturbations from a binary orbit may be detectable in pulsar timing residuals (e.g., PSR J0337+1715; Ransom et al. 2014). These perturbations were not found in the *RXTE* pulsar timing residuals reported in Pearlman et al. (2019), providing additional evidence against a third companion star.

4.4.3. Precession of the Donor Star

If a precessing donor star surrounded by an equatorially enhanced wind were the cause of the ~20.06 day period in IGR J16493-4348, long-term changes in the neutral hydrogen absorption column density may be observed (e.g., GX 304-1; Kühnel et al. 2017). We do not find any significant variations in $N_{\rm H}$ between superorbital minimum and maximum. However, we caution against ruling out a precessing equatorial wind since the absorbing material might not be along the line of sight.

4.4.4. Corotating Interaction Regions in the Stellar Wind

An alternative possibility is that the ~20.6 day cycle could be driven by large-scale corotating interaction regions (CIRs) in the wind of the B0.5 Ia donor star (Bozzo et al. 2017). Changes in the mass accretion rate may be partially modulated by the interaction between the neutron star and the CIRs. Phase-locked flares, possibly attributed to large-scale structures in the wind of the donor star, have been identified in the supergiant fast X-ray transient (SFXT) IGR J16479-4514 (Sidoli et al. 2013), which also shows strong superorbital modulation.

In a non-synchronous rotating binary, the angular velocities of the neutron star and the CIR would be different (see Bozzo et al. 2017 and references therein), resulting in a beat period on superorbital timescales. Bozzo et al. applied this model to IGR J16493-4348 and found that a single CIR with a period of ~10.3 days could explain the ~20.06 day superorbital period. We note the ~20.6 day modulation is persistently detected in

the dynamic power spectrum spanning a timescale of more than 12 yr (see Figure 2(a)). This suggests that, if CIRs are the cause of the superorbital modulation in these systems, they would have to be stable over timescales of several years (Pearlman et al. 2019).

4.4.5. Tidal Oscillations

Finally, we discuss the possible case that the superorbital modulation in IGR J16493-4348 is driven by a non-synchronously rotating donor star (Moreno et al. 2005; Koenigsberger et al. 2006), which could exhibit several different periodicities due to tidal oscillations (Zahn 1977; Moreno et al. 2005). Such oscillations could produce a localized structured wind, which would drive periodic modulation in the X-ray band when accreted onto the neutron star. The period of these oscillations was calculated to be on superorbital timescales for a circular orbit. From a pulsar timing analysis, Pearlman et al. (2019) showed that the binary is likely in a nearly circular orbit, which meets the requirement of the tidal oscillation model.

5. Summary and Conclusions

In this paper, we have presented two *NuSTAR* observations of IGR J16493-4348, which coincide with the minimum and maximum of one cycle of its ~20 day superorbital modulation, and long-term observations of the superorbital period by *Swift* BAT. An analysis of the BAT data using the dynamic power spectra and fractional rms methods reveals strong variations in the amplitude of the superorbital modulation, but we do not observe changes in the period. The fractional rms of the ~20.06 day period closely tracks the peak power, providing additional evidence that its amplitude significantly changes with time.

Our results indicate the neutron star rotation period is consistent with that reported by Pearlman et al. (2019) at the 1σ confidence interval. This suggests that no significant long-term neutron star rotation period derivative was detected between the *RXTE* and *NuSTAR* observations. No significant changes in the 3–50 keV pulse profiles between the two observations are found, which suggests a similar accretion regime at superorbital minimum and maximum.

We have presented a pulse-phase-resolved spectral analysis of IGR J16493-4348 for the first time. Our results show that, while the joint *NuSTAR* and *Swift* XRT pulse-phase-averaged spectral continuum revealed no significant changes between superorbital minimum and maximum, we observe possible evidence of luminosity-dependent variability in the pulse-phase-resolved spectra. We found the spectral shape near the broad main peak of the pulse profile hardens between superorbital minimum and superorbital maximum, which is consistent with the subcritical accretion regime. It may be possible that the spectral hardness evolution seen in IGR J16493-4348 could be explained by thermal Comptonization in a collisionless shock model (e.g., Cep X-4; Vybornov et al. 2017).

We also found a weak emission line at 6.4 keV at superorbital maximum, but it is not significant at superorbital minimum. The origin of the line is due to neutral Fe or Fe in a low ionization state, which is present in many X-ray binaries. Our pulse-phase-resolved analysis indicates that the flux of the Fe Kα line does not track the pulse profile, a possible indication that the region responsible for the Fe Kα emission is not close to the neutron star.

Our *NuSTAR* and *Swift* analysis shows that, while the mechanism responsible for the superorbital modulation remains elusive, we can now begin to constrain it. Mechanisms where we might expect a significant change in the neutral hydrogen column density—a precessing accretion disk, a precessing equatorially enhanced wind—are unlikely. A transient accretion disk may also be unlikely since the neutron star shows no indications of a rapid spin-up torque (Pearlman et al. 2019). A triple-star system is unlikely since the period of the third object is calculated to be 11.666 ± 0.002 days, which may lead to an unstable orbital configuration.

The superorbital dependence of the spectral shape in IGR J16493-4348, particularly near the broad main peak of the pulse profile, shows similarities to 2S 0114+650, which is the prototypical wind-fed SGXB exhibiting superorbital modulation (Farrell et al. 2006). While the spectral shape in each source hardens from superorbital minimum to maximum, an anticorrelation between photon index and X-ray luminosity is only observed in 2S 0114+650. The behavior of spectral hardness in both sources, however, may suggest that the superorbital mechanism is linked to a variable accretion rate. Superorbital mechanisms that explain the variable accretion rate such as tidal oscillations or large structures in the donor star wind remain possible.

To further understand the mechanism responsible for the ~20.06 day superorbital cycle in IGR J16493-4348, additional multi-wavelength observations are required. The study would benefit from optical/near-infrared photometry, which may confirm or preclude variations in the donor star or its wind as the driving mechanism of the superorbital modulation.

ORCID iDs

Joel B. Coley ● https://orcid.org/0000-0001-7532-8359
Robin H. D. Corbet ● https://orcid.org/0000-0002-3396-651X
Felix Fürst ● https://orcid.org/0000-0003-0388-0560
Hans A. Krimm ● https://orcid.org/0000-0003-4348-6058
Aaron B. Pearlman ● https://orcid.org/0000-0002-8912-0732
Katja Pottschmidt ● https://orcid.org/0000-0002-4656-6881

References

Bachetti, M., Harrison, F. A., Walton, D. J., et al. 2014, Natur, 514, 202
Ballhausen, R., Pottschmidt, K., Fürst, F., et al. 2017, A&A, 608, A105
Barthelmy, S. D., Barbier, L. M., Cummings, J. R., et al. 2005, SSRv, 120, 143

Becker, P. A., Klochkov, D., Schönherr, G., et al. 2012, A&A, 544, A123
Bird, A. J., Barlow, E. J., Bassani, L., et al. 2004, ApJL, 607, L33
Bondi, H., & Hoyle, F. 1944, MNRAS, 104, 273
Bozzo, E., Oskinova, L., Lobel, A., & Hamann, W.-R. 2017, A&A, 606, L10
Brightman, M., Harrison, F. A., Bachetti, M., et al. 2019, ApJ, 873, 115
Brumback, M. C., Hickox, R. C., Fürst, F. S., et al. 2018, ApJ, 852, 132
Burrows, D. N., Hill, J. E., Nousek, J. A., et al. 2005, SSRv, 120, 165
Capalbi, M., Perri, M., Saija, B., Tamburelli, F., & Angelini, L. 2005, The
  Swift XRT Data Reduction Guide, Technical Report 1.2, http://swift.gsfc.
  nasa.gov/analysis/xrt_swguide_v1_2.pdf
Chaty, S. 2011, in ASP Conf. Ser. 29, Evolution of Compact Binaries, ed.
  L. Schmidtobreick, M. R. Schreiber, & C. Tappert (San Francisco, CA:
  ASP), 447
Chou, Y., & Grindlay, J. E. 2001, ApJ, 563, 934
Clarkson, W. I., Charles, P. A., Coe, M. J., et al. 2003, MNRAS, 339, 447
Coburn, W., Heindl, W. A., Rothschild, R. E., et al. 2002, ApJ, 580, 394
Corbet, R., Markwardt, C., Barbier, L., et al. 2007, PThPS, 169, 200
Corbet, R. H. D., Barthelmy, S. D., Baumgartner, W. H., et al. 2010a, ATel,
  2599, 1
Corbet, R. H. D., Coley, J. B., & Krimm, H. A. 2017, ApJ, 846, 161
Corbet, R. H. D., Coley, J. B., Krimm, H. A., & Pottschmidt, K. 2018, ATel,
  11918, 1
Corbet, R. H. D., & Krimm, H. A. 2013, ApJ, 778, 45
Corbet, R. H. D., Pearlman, A. B., & Pottschmidt, K. 2010b, ATel, 2766, 1
Cusumano, G., La Parola, V., Segreto, A., et al. 2010, A&A, 510, A48
D'Aì, A., Cusumano, G., La Parola, V., et al. 2011, A&A, 532, A73
Dickey, J. M., & Lockman, F. J. 1990, ARA&A, 28, 215
El Mellah, I., Sander, A. A. C., Sundqvist, J. O., & Keppens, R. 2019, A&A,
  622, A189
Falkner, S., Schwarm, F.-W., Dauser, T., et al. 2019, A&A, submitted
Farrell, S. A., Sood, R. K., & O'Neill, P. M. 2006, MNRAS, 367, 1457
Farrell, S. A., Sood, R. K., O'Neill, P. M., & Dieters, S. 2008, MNRAS,
  389, 608
Fürst, F., Walton, D. J., Heida, M., et al. 2018, A&A, 616, A186
Fürst, F., Walton, D. J., Stern, D., et al. 2017, ApJ, 834, 77
Grebenev, S. A., Bird, A. J., Molkov, S. V., et al. 2005, ATel, 457, 1
Harrison, F. A., Craig, W. W., Christensen, F. E., et al. 2013, ApJ, 770, 103
Hill, A. B., Dean, A. J., Landi, R., et al. 2008, MNRAS, 385, 423
Hill, J. E., Burrows, D. N., Nousek, J. A., et al. 2004, Proc. SPIE, 5165, 217
Horne, J. H., & Baliunas, S. L. 1986, ApJ, 302, 757
Hu, C.-P., Chou, Y., Ng, C.-Y., Chun-Che Lin, L., & Chien-Chang Yen, D.
  2017, ApJ, 844, 16
Jenke, P. A., Finger, M. H., Wilson-Hodge, C. A., & Camero-Arranz, A. 2012,
  ApJ, 759, 124
Kalberla, P. M. W., Burton, W. B., Hartmann, D., et al. 2005, A&A, 440, 775
Klochkov, D., Staubert, R., Santangelo, A., Rothschild, R. E., & Ferrigno, C.
  2011, A&A, 532, A126
Klochkov, D. K., Shakura, N. I., Postnov, K. A., et al. 2006, AstL, 32, 804
Koen, C. 1990, ApJ, 348, 700
Koenigsberger, G., Georgiev, L., Moreno, E., et al. 2006, A&A, 458, 513

Kraus, U., Rebetzky, A., Herold, H., et al. 1989, in ESA Special Publications,
  Two Topics in X-Ray Astronomy, Vol. 1, ed. J. Hunt & B. Battrick
  (Noordwijk: ESA), 433
Krimm, H. A., Holland, S. T., Corbet, R. H. D., et al. 2013, ApJS, 209, 14
Kühnel, M., Falkner, S., Grossberger, C., et al. 2016, AcPol, 56, 41
Kühnel, M., Rothschild, R. E., Okazaki, A. T., et al. 2017, MNRAS, 471, 1553
Kuiper, L., Jonker, P., Hermsen, W., & O'Brien, K. 2005, ATel, 654, 1
Leahy, D. A. 1987, A&A, 180, 275
Makishima, K., Mihara, T., Nagase, F., & Tanaka, Y. 1999, ApJ, 525, 978
Markwardt, C. B., Swank, J. H., & Smith, E. 2005, ATel, 465, 1
Mazeh, T., & Shaham, J. 1979, A&A, 77, 145
Meszaros, P., & Nagel, W. 1985, ApJ, 299, 138
Mikkola, S. 2008, in Multiple Stars Across the H-R Diagram, ed. S. Hubrig,
  M. Petr-Gotzens, & A. Tokovinin (Berlin: Springer), 11
Molkov, S. V., Lutovinov, A. A., & Falanga, M. 2015, AstL, 41, 562
Moreno, E., Koenigsberger, G., & Toledano, O. 2005, A&A, 437, 641
Morris, D. C., Smith, R. K., Markwardt, C. B., et al. 2009, ApJ, 699, 892
Nespoli, E., Fabregat, J., & Mennickent, R. E. 2010, A&A, 516, A106
Ogilvie, G. I., & Dubus, G. 2001, MNRAS, 320, 485
Pearlman, A. B., Coley, J. B., Corbet, R. H. D., & Pottschmidt, K. 2019, ApJ,
  873, 86
Pike, S. N., Harrison, F. A., Bachetti, M., et al. 2019, ApJ, 875, 144
Postnov, K., Shakura, N., Staubert, R., et al. 2013, MNRAS, 435, 1147
Postnov, K. A., Gornostaev, M. I., Klochkov, D., et al. 2015, MNRAS, 452, 1601
Pringle, J. E. 1996, MNRAS, 281, 357
Protassov, R., van Dyk, D. A., Connors, A., Kashyap, V. L., &
  Siemiginowska, A. 2002, ApJ, 571, 545
Ramsay, G., Zane, S., Jimenez-Garate, M. A., den Herder, J.-W., &
  Hailey, C. J. 2002, MNRAS, 337, 1185
Ransom, S. M., Stairs, I. H., Archibald, A. M., et al. 2014, Natur, 505, 520
Reig, P., Chakrabarty, D., Coe, M. J., et al. 1996, A&A, 311, 879
Scargle, J. D. 1982, ApJ, 263, 835
Schwarm, F.-W., Ballhausen, R., Falkner, S., et al. 2017, A&A, 601, A99
Scott, D. M., Leahy, D. A., & Wilson, R. B. 2000, ApJ, 539, 392
Sidoli, L., Esposito, P., Sguera, V., et al. 2013, MNRAS, 429, 2763
Taani, A., Karino, S., Song, L., et al. 2019, RAA, 19, 012
Taani, A., Karino, S., Song, L., Zhang, C., & Chaty, S. 2018, arXiv:1808.05345
Tanaka, Y. 1986, LNP, 255, 198
Trowbridge, S., Nowak, M. A., & Wilms, J. 2007, ApJ, 670, 624
Tueller, J., Baumgartner, W. H., Markwardt, C. B., et al. 2010, ApJS, 186, 378
Vaughan, S., Edelson, R., Warwick, R. S., & Uttley, P. 2003, MNRAS, 345, 1271
Verner, D. A., Ferland, G. J., Korista, K. T., & Yakovlev, D. G. 1996, ApJ,
  465, 487
Vybornov, V., Klochkov, D., Gornostaev, M., et al. 2017, A&A, 601, A126
Walton, D. J., Fürst, F., Bachetti, M., et al. 2016, ApJL, 827, L13
White, N. E., Swank, J. H., & Holt, S. S. 1983, ApJ, 270, 711
Wilms, J., Allen, A., & McCray, R. 2000, ApJ, 542, 914
Winkler, C., Courvoisier, T. J.-L., Di Cocco, G., et al. 2003, A&A, 411, L1
Zahn, J.-P. 1977, A&A, 57, 383
Zdziarski, A. A., Wen, L., & Gierliński, M. 2007, MNRAS, 377, 1006